Contemporary Mathematics
http://ojs.wiserpub.com/index.php/CM/

Research Article

Numerical Computation and Statistical Interpretations of Heat Transfer of Tween-20/ethyl Acetate Nanofluid Flow with Melting Rheological Quality and Activation Energy

Aamir Farooq[1], Sadique Rehman[2], Mujahid Ullah[3], M. S. Abbas[4], K. El-Rashidy[5], M. Mamun Miah[2,6], Mohammad Kanan[7,8*]

[1] Department of Mathematics, Zhejiang Normal University, Jinhua 321004, PR China
[2] Division of Mathematical and Physical Sciences, Kanazawa University, Kakuma, Kanazawa 920-1192, Japan
[3] Department of Mathematics, University of Science and Technology, Bannu, Khyber Pakhtunkhwa, Pakistan
[4] Administrative and Financial Science Department, Ranyah University College, Taif University, Taif 21944, Saudi Arabia
[5] Technology and Science Department, Ranyah University College, Taif University,Taif 21944, Saudi Arabia
[6] Department of Mathematics, Khulna University of Engineering and Technology, Khulna-9203, Bangladesh
[7] Department of Industrial Engineering, College of Engineering, University of Business and Technology, Jed-dah, 21448, Saudi Arabia
[8] Department of Mechanical Engineering, College of Engineering, Zarqa University, Zarqa, Jordan
E-mail: m.kanan@ubt.edu.sa

Received: 29 July 2024; **Revised:** 18 August 2024; **Accepted:** 27 August 2024

Abstract: Tween-20 plays a significant role in the biological, food, and pharmaceutical industries. Additionally, it plays a vital role in improving the quality of reverse mechanisms of multi-drug resistance. This paper uses artificial neural computing to examine Tween-20 nanoparticles' behaviors in a base fluid called ethyl acetate to enhance the applications in nanomedicine, drug delivery and biotechnology. The study focuses on the nonlinear model of a viscous fluid at the stagnation point, where mixed convection processes and activation energy are present. The study incorporates slip velocity and melting boundary conditions to examine heat and mass transfer, taking into account thermal and solutal stratification. Various fields of research and technology, specially in industrial engineering that include hydrodynamics, panto-graph systems, and biomedical mathematics, extensively utilize artificial computing. The datasets are based on velocity, temperature, and concentration outlines. The fourth-order Runge-Kutta method is used to generate the datasets. To validate the LMM-ABNNs, we have compared them with a numerical solution, showing a high level of agreement. We utilize the error histogram and mean square error results to validate the performance, scrutinize the training and testing methods, and explore the validity of the approximate answer. Furthermore, the quality characteristics such as skin friction, rate of heat, and mass movement (Nusselt and Sherwood numbers) are statistically analyzed to forecast the model's durability. This article is the best example of investigating different fluid parameters with the latest artificial neural computing.

***Keywords*:** statistical interpretations, tween-20/ethyl acetate nanofluid, melting rheology, activation energy, artificial neural computing, numerical analysis, fourth-order runge-kutta method

MSC: 35C05, 35Qxx, 35J10, 34A25

DOI: https://doi.org/10.37256/cm.5420245398

1. Introduction

An artificial neural network (ANN) is a computational system composed of interconnected neurons that carry out information processing. It draws inspiration from biological neural networks. Weights in ANNs indicate the strength of connections between neurons. These weights are organized into layers (input, hidden, and output) and play a crucial role in facilitating learning and acquiring knowledge. The neurons in the network generate output values by nonlinearly altering input data, enabling categorization and function approximation. Training an ANN involves assigning input patterns to anticipated output patterns. An application uses the trained network to predict outputs for new input patterns. ANNs introduce nonlinearity into calculations and optimize network parameters to improve performance by utilizing activation functions, such as piecewise linear functions. ANNs are critical for advancing fluid mechanics research. They have several applications, such as predicting gradients and objective function values in optimization problems [1]. Furthermore, physics-informed machine-learning (PIML) methods combine ML algorithms with domain knowledge to improve the reliability and effectiveness of predicting complex turbulent flows in fluid mechanics [2]. ANNs have significantly influenced experimental fluid dynamics by enabling real-time estimation and control, enhancing experimental design, and improving measurement techniques. These advancements have increased accuracy and excellence in the field [3, 4]. Using ANNs in fluid dynamics, research showcases the potential for advanced advancements and applications in engineering, science, and healthcare. In their study, Rehman et al. [5] used ANNs to examine how cross-nanofluids move when an inclined magnetic field and a heat source exist. Ali et al. [6] investigated the characteristics of unsteady hydromagnetic flow through an angular rotating disk using artificial neural computing. More research using ANNs is being done to examine how magnetic fields, heat transfer, entropy generation, and different kinds of nanoparticles affect the flow of nanofluids. It can be found in [7–10]. We have utilized the ANNs to investigate the behavior of viscous nanofluid flow under the influence of an angled magnetic field.

Nanofluids are novel heat transfer fluids with improved thermal properties of nanoparticles scattered throughout base fluids. Even at modest nanoparticle concentrations, these colloidal solutions have demonstrated impressive enhancement in the thermal conductivity of the base fluid. [11]. Nanofluids find significance in different sectors like cooling systems, solar panels, and CO_2 absorption because of their remarkable thermophysical properties. The preparation procedures include synthesizing nanoparticles and applying methods such as ultrasonication to increase thermophysical properties and stability [12]. Understanding the behavior of nanofluids requires a grasp of physicochemical concepts such as surface-to-volume ratio, Brownian movement, electrical effects, and nanoparticle aggregation. Farooq et al. [13] explored the oscillatory behavior of Maxwell nanofluid with heat and mass transport, utilizing the Laplace transform to acquire the closed-form solution of the model. Asgar et al. [14] investigate thermal characterization of hybrid nanofluid with impact of convective boundary layer flow and Joule heating law. Lin et al. [15] demonstrated the effects of free convective behavior of fractional nanofluid flow with heat source/sink via porous medium. Hussain et al. [16] scrutinized the behavior of zinc oxide and zirconium oxide impacts on hybrid nanofluid (kerosene oil) flow between two porous and squeezing rotating discs. Shah et al. [17] discoursed a numerical study of hybrid nanofluid flow through power law shrinking/stretching sheet with radiation and suction effects. Lund et al. [18] presented the dual solution of MHD hybrid nanofluid flow via Darcy-Forchheimer medium with the impact of joule heating and viscous dissipation. Rasool et al. [19] investigated the MHD radiating thixotropic nanofluid flow over an extended sheet with convected conditions. Further studies on Newtonian and non-Newtonian nanofluid flow can be done in [20–24].

Stratification is the emergence of layers of fluid with varying densities. This density variation results from variations in the temperature or concentration of the fluid's reservoirs. It is frequently employed in processes related to industry, biomedicine, agriculture, and the environment. A few instances of stratification include heterogeneous combinations in the atmosphere, reservoirs, and oceans. It also plays a big part in regulating the amounts of hydrogen and oxygen in the atmosphere and oceans. It mostly affects the amount of algae, the quality of the water, and the lack of oxygen in the lower reaches of ponds, lakes, and rivers. Raizah et al. [25] investigated the impacts of third-grade nanofluid flow with melting phenomenon and temperature stratification over a Riga plate in the presence of stagnation point. Lone et al. [26] scrutinized the temperature and concentration stratification in Casson nanofluid flow with the impacts of microorganisms via a 3D bi-stretching sheet. Ganie et al. [27] studied the radiated Maxwell nanofluid with melting rheology and dual

quadratic stratification having joule heating via an extended sheet. Algehyne et al. [28] analyzed thermally stratified Carreau-Yasuda nanofluid flow behavior with Cattaneo-Christov heat flux, Brownian, and thermophoretic phenomenon. The analytical solution is acquired via the homotopy analysis method (HAM). Zafar et al. [29] demonstrated the dual stratification effects in Ree-Eyring nanofluid flow with gyrotactic microorganisms via a Darcy Forchheimer medium. Entropy generation is also presented with radiation and heat source/sink. Leng et al. [30] proposed the numerical solution of MHD thermally stratified Casson nanofluid flow with heat suction/injection properties and joule heating via a Darcy Forchheimer permeable medium. Debnath et al. [31] analyzed numerically on heat transfer enhancement and design optimization of modified SCTHX using Taguchi method. Das et al. [32] depicted the irreversible behavior of triply stratified Powell-Eyring nanofluid flow with bio-Marangoni convection condition. So, we have also accounted for the dual stratification effects on viscous nanofluid flow with melting and slip conditions.

Scientists have observed a significant need for power storage technologies that offer increased durability and reliability. Battery storage systems are essential for reactor designs used in heating, wind power, mixed energy generation, and waste-to-energy recovery. Latent heat storage is a method of storing energy. Latent thermal energy storage is a highly efficient and cost-effective energy storage method. One way to store thermal energy in a substance is to cause it to melt. We solidify the material to release the accumulated heat energy. The melting impacts encompass a variety of processes, including semiconducting operations, tundra melting, magma solidification, and freezing heat exchanger coils in a ground-based pump. The mixed convection viscous nanofluid flow via an inclined sheet with stagnation point, melting rheology, and variable porosity and permeability have not been explored as far as the authors know. The model considers the effects of thermal and solutal stratification and the influence of activation energy and joule heating. The base fluid, ethyl acetate, creates a uniform mixture by immersing Tween-20 nanoparticles. We obtain the numerical solution using the fourth-order Runge-Kutta method and then compare it with the results obtained via ANN computation. We examine the validation of the approximation solution using error histograms and mean square error results to assess performance and analyze training and testing procedures. In addition, probable error and multilinear regression methods are utilized to establish a correlation between the different embedded factors, specifically drag force, rate of heat, and mass transfer. Existing theoretical models cannot accurately predict the behavior of such nanofluids under dynamic conditions. Refining or developing new models is necessary to investigate such types of characteristics. Our proposed model would be an excellent example to explain suchtypes of explanation.

2. Mathematical modeling

A two-dimensional viscous fluid flow through a porous region that is non-Darcy saturated is considered. An incompressible fluid saturates a semi-infinite region enclosed by a continuously moving stretching sheet. Heat transmission characteristics have been set out by variables such as heat generation/absorption and variable thermal conductivity. It applies a magnetic field angled α to the stretching surface. Due to the low magnetic Reynolds number, the induced magnetic field is ignored. Under the boundary layer, the continuity, momentum, energy, and concentration equations are given [33, 34].

$$\frac{\partial u}{\partial x}+\frac{\partial v}{\partial y}=0, \tag{1}$$

$$\rho_{nf}(u\frac{\partial u}{\partial x}+v\frac{\partial u}{\partial y})=\mu_{nf}\frac{\partial^2 u}{\partial y^2}-\frac{\mu_{nf}\varepsilon(y)}{K(y)}u-\frac{\rho_{nf}C_b\varepsilon^2(y)}{\sqrt{K(y)}}u^2-\sigma_{nf}sin^2(\alpha)B_0^2(u-U_\infty)$$

$$+\rho_{nf}U_\infty\frac{dU_\infty}{dx}+g(\rho\beta_T)_{nf}cos(\beta)(T-T_m), \tag{2}$$

$$(\rho C_p)_{nf}(u\frac{\partial T}{\partial x}+v\frac{\partial T}{\partial y})=K_{nf}\frac{\partial^2 T}{\partial y^2}+\mu_{nf}(\frac{\partial u}{\partial y})^2+Q_0(T-T_m) \tag{3}$$

$$+\sigma_{nf}sin^2(\alpha)B_0^2(u-U_\infty)^2,$$

$$u\frac{\partial C}{\partial x}+v\frac{\partial C}{\partial y}=D_m\frac{\partial^2 C}{\partial y^2}-K_B^*(\frac{T}{T_\infty})^n exp[\frac{-E_a}{kT}](C-C_m), \tag{4}$$

with the boundary conditions

$$u=U_w(x)=ax+N\frac{\partial u}{\partial y},\quad T=T_m, C=C_m\ as\ y\to 0 \tag{5}$$

$$u=U_\infty(x)=bx, T=T_\infty,\quad C=C_\infty\ as\ y\to\infty \tag{6}$$

$$K_{nf}\frac{\partial T}{\partial y}|_{y=0}=\rho_{nf}[\lambda+C_s(T_m-T_0)]v(x,0) \tag{7}$$

where, $T_m=T_0+d_1x^3$, $T_\infty=T_0+d_2x^3$, $C_m=C_0+e_1x^3$, $C_\infty=C_0+e_2x^3$.

In this case, u and v stand for the horizontal and vertical components of velocity, respectively, as well as ρ fluid density, ρ_{nf} density of nanofluid, μ_{nf} viscosity of nanofluid,$\varepsilon(y)$ and $K(y)$ are porosity and permeability of the porous medium, respectively, σ_{nf} permeability of nanofluid, C_b inertia coefficient, B_0 field strength, C_p specific heat, U_∞ fluid velocity outside boundary layer, g acceleration due to gravity, $\beta_{T_{nf}}$ thermal expansion, $\beta_{C_{nf}}$ solutal expansion of nanofluid, K_{nf} thermal conductivity of nanofluid, Q_0 coefficient of heat generation/absorption, D_m mass diffusivity, K_B^* chemical reaction rate, Ea activation energy,λ thermal conductivity.

The porosity, $\varepsilon(y)$ and permeability, $K(y)$ are defined by follows,

$$\varepsilon(y)=\varepsilon_0(1+b_1e^{-\eta}), \tag{8}$$

$$K(y)=K_0(1+be^{-\eta}), \tag{9}$$

the porosity and permeability at the boundary layer's edge are denoted by ε_0 and K_0. While $b_1=b=0$ for uniform permeability (see [35]), the variable porosity and permeability values are 1.5 and 3.0, respectively.

The transformation variables are defined as follows,

$$\eta = y\sqrt{\frac{a}{\nu_f}}, \quad u = axf^{'}(\eta), \quad v = -\sqrt{a\nu_f}f(\eta),$$

$$\theta(\eta) = \frac{T - T_m}{T_\infty - T_0}, \quad \phi(\eta) = \frac{C - C_m}{C_\infty - C_0}, \tag{10}$$

where ν_f kinematic viscosity of a fluid. Since Eq. 1 automatically satisfied by using Eq. (10) and other equations from Eq. (2)-Eq. (4) converted as follows,

$$a_1(f^{'2} - ff^{''}) = \frac{f^{'''}}{(1-\varphi)^{2.5}} - \frac{1}{(1-\varphi)^{2.5}}\frac{1}{\sigma Re}\frac{(1+b_1e^{-\eta})}{(1+be^{-\eta})}f^{'}$$

$$- a_1\beta^*\frac{(1+b_1e^{-\eta})^2}{\sqrt{(1+be^{-\eta})}}f^{'2} - c_3M^2sin^2(\alpha)(f^{'} - S) + S^2 + Gr_Ta_1c_1\theta cos(\beta), \tag{11}$$

$$a_2(3f^{'}\theta + 3Af^{'} - f\theta^{'}) = \frac{c_4}{Pr}\theta^{''} + \frac{1}{(1-\varphi)^{2.5}}Ecf^{''2} \tag{12}$$

$$+ \delta_1\theta + c_3sin^2(\alpha)EcM^2(f^{'} - S)^2,$$

$$3f^{'}\phi + 3A_1f^{'} - f\phi^{'} = \frac{1}{Sc}\phi^{''} - \gamma_1((\theta\sigma_1 + 1)\gamma)^n exp[\frac{-E_a}{1+\sigma_1\theta}]\phi. \tag{13}$$

The boundary conditions (Eq. (5)-Eq. (7)) are converted as the following forms,

$$f'(0) = 1 + N^*f^{''}(0), \quad \theta(0) = 0, \quad \phi(0) = 0 \text{ as } \eta \to 0, \tag{14}$$

$$f^{'}(\infty) = S, \quad \theta(\infty) = 1 - A \text{ and } \phi(\infty) = 1 - A_1 \text{ as } \eta \to \infty, \tag{15}$$

$$Prf(0) + \frac{c_4}{a_1}M_1\theta^{'}(0) = 0 \text{ as } \eta \to 0. \tag{16}$$

Here some parameters which are used to conversion, density $\rho_{nf} = (1-\varphi)\rho_f + \varphi\rho_s$, $a_1 = (1-\varphi) + \varphi\frac{\rho_s}{\rho_f}$, $a_2 = (1-\varphi) + \varphi\frac{(\rho C_p)_s}{(\rho C_p)_f}$, $c_1 = (1-\varphi) + \varphi\frac{\beta_{T_s}}{\beta_{T_f}}$, $c_3 = \frac{\sigma_{nf}}{\sigma_f} = 1 - \frac{3\varphi(1-\frac{\sigma_s}{\sigma_f})}{(2+\frac{\sigma_s}{\sigma_f}) + \varphi(1-\frac{\sigma_s}{\sigma_f})}$, $c_4 = \frac{k_{nf}}{k_f} = \frac{2k_s + 2k_f - 2\varphi(k_f - k_s)}{k_s + 2k_f + \varphi(k_f - k_s)}$, kinematic viscosity, $\nu = \frac{\mu}{\rho}$, local inertial parameter, $\beta^* = \frac{C_b\varepsilon_0^2}{\sqrt{k_0}}$, local magnetic parameter, $M^2 = \frac{\sigma_f B_0^2}{\rho_f a}$, dynamic viscosity $\mu_{nf} = \frac{\mu_f}{(1-\varphi)^{2.5}}$, ratio parameter, $S = \frac{b}{a}$, Grashof number for temperature, $Gr_T = \frac{g\beta_{T_f}(T_\infty - T_0)}{aU_w}$, local permeability

parameter, $\sigma = \frac{k_0 a^2}{U_w^2 \varepsilon_0}$, local Reynolds number, $Re = \frac{U_w x}{\nu_f}$, Prandtle number, $Pr = \frac{(\mu C_p)_f}{k_f}$, thermal stratification, A, ratio parameter, $B_2 = \frac{K_{nf}}{K_f}$, Eckert number, $Ec = \frac{U_w^2}{C_{p_f}(T_\infty - T_0)}$, heat source/sink, $\delta_1 = \frac{Q_0}{a(\rho C_p)_f}$, Schmidt number, $Sc = \frac{\nu_f}{D_m}$, chemical reaction parameter, $\gamma_1 = \frac{K_B^*}{a}$, material parameter, $\gamma = \frac{T_m}{T_\infty}$, material parameter, $\sigma_1 = \frac{T_\infty - T_0}{T_m}$, activation energy, $E = \frac{Ea}{kT_m}$, material parameter, N^*, solutal stratification, A_1, melting parameter, $M_1 = \frac{C_{p_f}(T_\infty - T_0)}{\lambda + C_s(T_m - T_0)}$.

The temperature gradient (Nusselt number) at the wall of the stretching sheet, the velocity gradient (skin friction or drag force) at the normal surface, and the Sherwood number are the engineering interest quantities are defined as follows,

$$C_f = \frac{\tau_m}{\rho U_m^2}, \quad Nu_x = \frac{x q_m}{k_f(T_\infty - T_m)}, \quad Sh_x = \frac{x q_s}{D_B(C_\infty - C_m)}, \tag{17}$$

where τ_m, q_m, and q_s are known as the wall shear stress, the surface heat flux, and the wall mass flux, respectively, and are defined as follows,

$$\tau_m = \mu(\frac{\partial u}{\partial y})_{y=0}, \quad q_m = -k_{nf}(\frac{\partial T}{\partial y})_{y=0}, \quad q_s = -D_B(\frac{\partial C}{\partial y})_{y=0}. \tag{18}$$

Using the variable transformations Eq. (10), we obtain the ordinary differential equation for skin friction, Nusselt number, and Sherwood number, respectively,

$$C_f\sqrt{Re_x} = f''(0), \; -Nu_x Re_x^{-\frac{1}{2}} = \frac{c_4\theta'(0)}{1-A} \text{ and } -Sh_x Re_x^{-\frac{1}{2}} = \frac{\phi'(0)}{1-A_1}.$$

3. Methodology

The first section explains the process of creating a dataset for (11)-(16). The second section outlines the exact processes utilized to implement the dataset. An efficient, competent, and adept technique in the artificial neural networks toolbox developed in MATLAB, the fitting tool "nftool" plays an important role in the simulation of the planned model. The suggested model combines a multi-layer neural network architecture with backpropagated neural networks that use a Levenberg Marquard topology to improve it. The results of numerical experiments for the dynamics indicated in (11)-(16) are presented here, along with the important justification for the developed model.

In MATLAB, for each scenario of a model, four different cases are shown in Tables 1-6. The reference dataset for velocity, temperature, and concentration profiles is established using the fourth-order Runge Kutta method approach. The cases of model are represented in (11)-(16). The input data ranges from 0 to 1, with intervals of 0.001. The reference results utilized throughout this paper are generated by applying the fourth-order Runge-Kutta algorithm to the dataset containing velocity, temperature, and concentration profiles. For 1,000 input points, 70% of the input values are used for training, 15% for validation, and 15% for testing. The reference results for the velocity profile and temperature profile are established. Figure 1 displays the schematic diagram of the neural network's structure. The proposed approach, called LMM-ABNNs, is applied to six physical parameters. The parameters G_{rt}, M_1, ϕ, S, Ec, and Sc are varied in four separate scenarios, and equations (11)-(16) are used. The specific values used are presented in Tables 1-6.

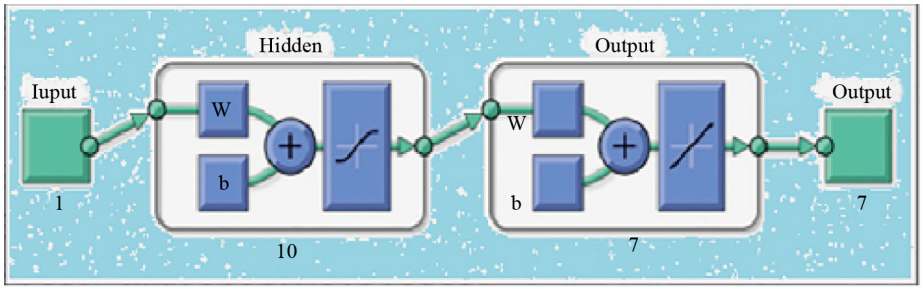

Figure 1. Schematic diagram (in ref. [36]) of the neural network's structure

Table 1. Results of NN-BLMS for G_{rt}

G_{rt}	Mean square error			Performance	Gradient	μ	Epoch	Time (seconds)
	Training	Validation	Testing					
1	2.4e-07	1.4e-04	3.3e-06	1.04e-08	4.97e-05	1e-8	1,000	10
10	3.4e-08	2.7e-05	3.8e-05	1.71e-08	1.35e-5	1e-7	1,000	09
20	1e-08	3.1e-07	1.6e-05	2.88e-08	7.6e-06	1e-7	1,000	10
50	3.4e-05	8.7e-04	3.7e-04	2.96e-05	1.87e-03	1e-5	125	06

Table 2. Results of NN-BLMS for M_1

M_1	Mean square error			Performance	Gradient	μ	Epoch	Time (seconds)
	Training	Validation	Testing					
0.1	6.7e-09	6.1e-05	7.7e-05	5.23e-08	2.91e-05	1e-7	788	06
0.5	1.6e-08	2e-04	8.2e-05	2.16e-08	5.8e-6	1e-7	1,000	10
0.9	1.8e-07	2.2e-04	1.1e-04	1.22e-07	2.61e-05	1e-6	1,000	12
1.3	4.2e-08	1.1e-04	8.6e-06	1.15e-08	1.73e-05	1e-7	1,000	11

Table 3. Results of NN-BLMS for ϕ

ϕ	Mean square error			Performance	Gradient	μ	Epoch	Time (seconds)
	Training	Validation	Testing					
0.001	3.9e-08	1.3e-05	2.1e-04	3.14e-09	1.36e-05	1e-8	1,000	07
0.006	6.6e-08	1.4e-04	2.9e-05	1.91e-07	3.41e-5	1e-7	1,000	10
0.01	2.67e-09	2.4e-04	1.6e-04	4.36e-07	2.58e-05	1e-6	1,000	10
0.06	2.8e-08	2.3e-05	1.1e-05	2.12e-08	1.25e-05	1e-7	1,000	1.21

Table 4. Results of NN-BLMS for S

S	Mean square error			Performance	Gradient	μ	Epoch	Time (seconds)
	Training	Validation	Testing					
0.1	1.1e-06	2e-06	3.4e-06	1.42e-08	2.09e-04	1e-8	1,000	14
0.5	1.8e-08	3e-04	9.7e-04	3.72e-08	5.5e-6	1e-7	1,000	08
0.9	3.6e-08	1.8e-06	4e-06	2.08e-09	9.96e-08	1e-8	387	08
1.3	3.2e-08	8.4e-07	1.8e-06	2.41e-09	9.98e-08	1e-8	343	07

Table 5. Results of NN-BLMS for Ec

Ec	Mean square error			Performance	Gradient	μ	Epoch	Time (seconds)
	Training	Validation	Testing					
0.1	2.6e-08	3.2e-06	9.4e-06	8.43e-08	1.18e-05	1e-8	1,000	14
0.2	3.2e-06	2.4e-05	1.2e-07	1.21e-07	2.03e-5	1e-7	867	06
0.3	2.6e-08	1.3e-04	1.5e-04	9.06e-07	2.79e-05	1e-8	1,000	07
0.4	9.4e-08	1.9e-02	8.9e-04	2.59e-07	9.32e-05	1e-8	1,000	07

Table 6. Results of NN-BLMS for Sc

Sc	Mean square error			Performance	Gradient	μ	Epoch	Time (seconds)
	Training	Validation	Testing					
0.1	5.6e-08	2.1e-05	1.9e-05	9.51e-09	3.08e-05	1e-8	1,000	08
0.6	2.5e-06	1.1e-04	1.6e-05	2.5e-07	8.58e-4	1e-7	518	07
1.2	2.5e-08	3.7e-05	1.1e-04	8.68e-09	1.56e-05	1e-8	1,000	07
2	2.4e-09	3.3e-06	1.4e-04	4.05e-09	6.88e-06	1e-8	1,000	08

4. Statistical analysis

We will look at skin friction, Nusselt number, and Sherwood number with the help of correlation coefficients, probable errors, and the absolute ratio of correlation coefficient to probable error. To achieve this goal, we have prepared Tables 7-9 that will be used to determine the correlation coefficient. The correlation coefficient is essential for determining any connection's strength and direction.

Table 7. Correlation coefficient (r), probable error (PE), and $|\frac{r}{PE}|$ values of skin friction

Parameters	r	PE	$\lvert\frac{r}{PE}\rvert$
α	-0.067038	0.122593	0.546837
G_{rt}	1.000000	0.000000	∞
G_{rc}	1.000000	0.000000	∞
M^2	-0.975167	0.006040	161.443678
M_1	0.999458	0.000134	7483.660724
ϕ	-0.999793	0.000051	19632.366023

Table 8. Correlation coefficient (r), probable error (PE), and $|\frac{r}{PE}|$ values of Nusslet number

Parameters	r	PE	$\lvert\frac{r}{PE}\rvert$
α	-0.936956	0.015038	62.306826
S	0.992784	0.001771	560.630031
ϕ	-0.153425	0.131255	2.550797
M^2	-0.975893	0.005866	166.367674
M_1	0.992978	0.001723	576.179117
Ec	-1.000000	0.000000	∞
A	0.999995	0.000001	887351.829991

Table 9. Correlation coefficient (r), probable error (PE), and $|\frac{r}{PE}|$ values of Nusslet number

Parameters	r	PE	$\lvert\frac{r}{PE}\rvert$
E	-0.339702	0.108936	3.118379
Sc	0.999948	0.000013	78326.201362
A_1	0.989431	0.002589	382.121283
γ_1	0.990816	0.002252	440.043203

4.1 *Probable error and correlation coefficient*

Here, the correlation coefficient, the probable error (PE), and the absolute value of the ratio, $|\frac{r}{PE}|$ for skin fraction, Nusselt number, and Sherwood number are provided in Tables 7-9 respectively. The correlation coefficient is used to compute the probable error. These computations are essential to ensure the correlation coefficient values are precise and accurate. The probable error is defined as follows,

$$PE = \frac{1-r^2}{\sqrt{n}}0.6745$$

where r stands for the correlation coefficient and n stands for number of observations.

4.2 *Multiple linear regression*

The connection between the extract (the dependent variable) and one or more predictors (the independent variables) is evaluated using linear regression analysis. Multiple regression analysis is used to estimates $Cf_xRe_x^{\frac{1}{2}}$, $Nu_xRe_x^{-\frac{1}{2}}$, and $Sh_xRe_x^{-\frac{1}{2}}$ and obtained all correlations are significant. The suggested models' general forms are provided by:

$$Cf_{est} = a_0 + a_\alpha\alpha + a_{G_{rc}}G_{rc} + a_{G_{rt}}G_{rt} + a_{M^2}M^2 + a_{M_1}M_1 + a_\phi\phi,$$

$$Nu_{est} = b_0 + b_\alpha\alpha + b_S S + b_{M^2}M^2 + b_{M_1}M_1 + b_\phi\phi + b_{Ec}Ec + b_A A,$$

$$Sh_{est} = c_0 + c_E E + c_{Sc} Sc + c_{A_1} A_1 + c_{\gamma_1} \gamma_1,$$

where the confidence intervals for coefficients are, $a_0 \in (-4.6135,\ -4.1712)$, $a_\alpha \in (-0.0024,\ 0.0008)$, $a_{G_{rt}} \in (-0.0260,\ 0.0253)$, $a_{G_{rc}} \in (-0.0093,\ 0.0409)$, $a_{M^2} \in (-0.0766,\ -0.0265)$, $a_{M_1} \in (0.2441,\ 0.9630)$, $a_\phi \in (-13.7202,\ -8.6339)$, $b_0 \in (-0.8010,\ -0.1836)$, $b_\alpha \in (-0.0017,\ 0.0023)$, $b_S \in (-0.9393,\ -0.0839)$, $b_{M^2} \in (-0.0921,\ -0.0147)$, $b_{M_1} \in (0.7353,\ 1.6844)$, $b_\phi \in (-7.6003,\ -0.6285)$, $b_{Ec} \in (-0.3657,\ -0.2947)$, $b_A \in (-2.1305,\ -1.1711)$, $c_0 \in (-1.0127,\ -1.0046)$, $c_E \in (-0.0002,\ 0.0001)$, $c_{Sc} \in (0.2718,\ 0.3071)$, $c_{A_1} \in (0.0563,\ 0.0910)$ and $c_{\gamma_1} \in (-0.0285,\ -0.0027)$.

Using these confidence levels of intervals for coefficients, we estimate the following:

$$Cf_{est} = -4.3924 - 0.0008\alpha - 0.0004G_{rc} + 0.0158G_{rt} - 0.0516M^2 + 0.6036M_1 - 11.1771\phi,$$

$$Nu_{est} = -0.4923 + 0.0003\alpha - 0.5116S - 0.0534M^2 + 1.2098M_1 - 4.1144\phi - 0.3302Ec - 1.6508A,$$

$$Sh_{est} = -1.0127 - 0.0001E + 0.2895Sc + 0.0736A_1 - 0.0156\gamma_1.$$

When a parameter has a positive sign in the estimated regression coefficient, it indicates that the drag coefficient, the heat transfer rate, and the mass transfer rate are rising. When it has a negative sign, it indicates that the drag coefficient, the heat transfer rate, and the mass transfer rate are falling. From the first mentioned models, we observed that the drag coefficient goes down with increasing α, G_{rc}, M^2, ϕ and goes up with augmentation in G_{rt} and M_1. For the second mentioned model, we observed that the heat transfer rate decreases with increasing S, M^2, ϕ, Ec, A and increases with augmentation in α and M_1. For the last linear regression model, the mass transfer rate goes down with increasing E, γ_1, and goes up with augmentation in Sc and A_1. Through Figures 8(a-c), the predicted regression model's accuracy (for the selected sample) has been determined. Tables 7-9 show similar output with our extracted results.

For three cases, the values of R-square, F-statistic, P-value, and error variance estimate are given in Table 10. The study of the drag coefficient revealed that our projected model performed well, as evidenced by R-square values of (0.85115). Additionally, the model's reliability was confirmed by the F-statistic of (21.9195), which is unusually high, the low values of P-values ($1.9276E-08$), and the significant level of precision for the error variance estimate (0.00944455). The Nusselt number revealed that our model performed highly, as evidenced by R-square values of (0.95373). Additionally, the model's reliability was confirmed by the F-statistic of (64.7794), which is unusually high, the low values of P-values ($3.2518E-13$), and the significant level of precision for the error variance estimate (0.014868). Based on the Sherwood number study, the high performance of the projected model is evidenced by R-square values of 0.98097. The model's reliability is also supported by the model's unusually high F-statistic of 322.1138, low P-value of $4.1369E-21$, and significant precision for the error variance estimate of $2.8761E-05$.

Table 10. Statistical parameters

Parameters	R-square	F-statistic	P-value	Error variance estimate
Cf_{est}	0.85115	21.9195	1.9276E-08	0.00944455
Nu_{est}	0.95373	64.7794	3.2518E-13	0.014868
Sh_{est}	0.98097	322.1138	4.1369E-21	2.8761E-05

5. Results and discussion

The primary goal of our article is to use ANNs to examine the effects of an angled magnetic field across a non-Darcy-saturated porous region. We used the LMM-ABNNs model to examine the importance of various parameters on the mentioned stretching surface. Here we mention comparison and error analysis of the LMM-ABNNs model with numerical results for G_{rt}, M_1, ϕ, S, Ec, and Sc in the following:

In Figure 2, the velocity distribution increased as the Grashof number, which gives us the buoyancy force becomes more dominant than the viscous force of the non-Darcy saturated porous region are plotted in Figure 2a, in Figure 2b shows that increasing of Grashof number, the error fluctuation is increasing proportionally, the best performance recorded $2.545e-08$ at epochs 1,000 with the MSE $e-08$ are plotted in Figure 2c, corresponding gradient and Mu are around $1.3547e-05$ and $1.0e-07$ respectively in Figure 2d, Figure 2e gives error histogram of each input point with zero line has error $-4.9e-06$, the height error for different data is $5e-05$ in Figure 2f, lastly the results of regression analysis are given in Figure 2g. In Figure 2, all comparisons are depicted due to the Grashof number.

In Figure 3, the velocity distribution increased as the melting parameter, which shows that the convection phenomena is dominant, which means that the more energetic particles move quickly from heated liquid to the cold melting surface are plotted in Figure 3a, 3b shows that increasing of melting parameter, the error fluctuation is increasing proportionally, in Figure 3c shows the temperature distribution is decreasing due to increasing of melting parameter because the heat diffuses more rapidly toward cold wall. Thus, the temperature is reduced. In Figure 3d, the error fluctuation increases proportionally due to the melting parameter. The best performance recorded $3.2014e-07$ at epochs 782 with the MSE $e-06$ are plotted in Figure 3e, corresponding gradient and μ are around $2.9125e-05$ and $1.0e-07$ respectively in Figure 3f. Figure 3g gives an error histogram with zero line has error $-1.8e-04$, the height error for different data is $5e-05$ in Figure 3h, lastly, the results of regression analysis are given in Figure 3i.

In Figure 4, the velocity distribution decreased with increasing nanoparticle concentration, plotted in Figure 4a. Physically, enhancing nanoparticle volume dominates the viscosity of the liquid. Therefore, the nanofluid's velocity reduces. Figure 4b shows that the error fluctuation increases proportionally with increasing nanoparticle volume. Figure 4c shows the temperature distribution is increasing due to the increasing of nanoparticles volume fraction parameter because the collision between the particles enhances that produces more heat. Figure 4d, the error fluctuation is increasing proportionally. The best performance recorded $8.9602e-09$ at epochs $1,000$ with the MSE $e-08$ in Figure 4e and corresponding gradient and μ are $1.3612e-05$ and $1.0e-08$ respectively in Figure 4f at $1,000$ epochs. Figure 4g gives an error histogram with zero line has error $-8.3e-05$, the height error for different data is $1.0e-05$ in Figure 4h, lastly the results of regression analysis in Figure 4i.

In Figure 5, the velocity distribution increased with the increasing of ratio parameters, which are plotted in Figure 5a and 5b shows that with increasing ratio parameters, the error fluctuation increases proportionally. Figure 5c shows the temperature distribution is increasing due to the increasing of ratio parameter, and Figure 5d the error fluctuation is decreasing proportionally. The best performance recorded $6.9039e-09$ at epochs $1,000$ with the MSE $e-08$ in Figure 5e and corresponding gradient and μ are $2.0918e-04$ and $1.0e-08$ respectively in Figure 5f at $1,000$ epochs. 5g gives an error histogram with zero line has error $-2.2e-05$, the height error for different data is $5.0e-05$ in Figure 5h, lastly the results of regression analysis in Figure 5i.

In Figure 6, the temperature distribution increased with the increasing of Eckert number in Figure 6a. Physically, the resistive force between the particles generates more heat. Thus, temperature elevates. Figure 6b shows the absolute error between the numerical and ANNs method. The best performance recorded $5.7938e-08$ at epochs 861 with the MSE $e-08$ in Figure 6c and corresponding gradient and μ are $2.0328e-05$ and $1.0e-07$ respectively in Figure 6d at 867 epochs. Figure 6e gives an error histogram with zero line has error $-1.8e-05$, the height error for different data is $1.0e-04$ in Figure 6f, lastly, the results of regression analysis in Figure 6g.

In Figure 7, the concentration distribution decreases as the Schmidt number increases. Figure 7a. Physically, as the Schmidt number elevates, the concentration reduces because mass diffusivity is more dominant than momentum diffusivity. and Figure 7b shows the absolute error. The best performance recorded $2.5815e-08$ at epochs $1,000$ with the MSE $e-07$ in Figure Figure 7c and corresponding gradient and μ are $3.0771e-05$ and $1.0e-08$ respectively in Figure 7d at $1,000$

epochs. Figure 7e gives an error histogram with zero line has error $1.24e-05$, the height error for different data is $2.0e-05$ in Figure 7f, lastly, the results of regression analysis in Figure 7g.

Through figures 8a-c, the estimated regression model's accuracy has been determined. The agreement between the estimated and actual values is excellent.

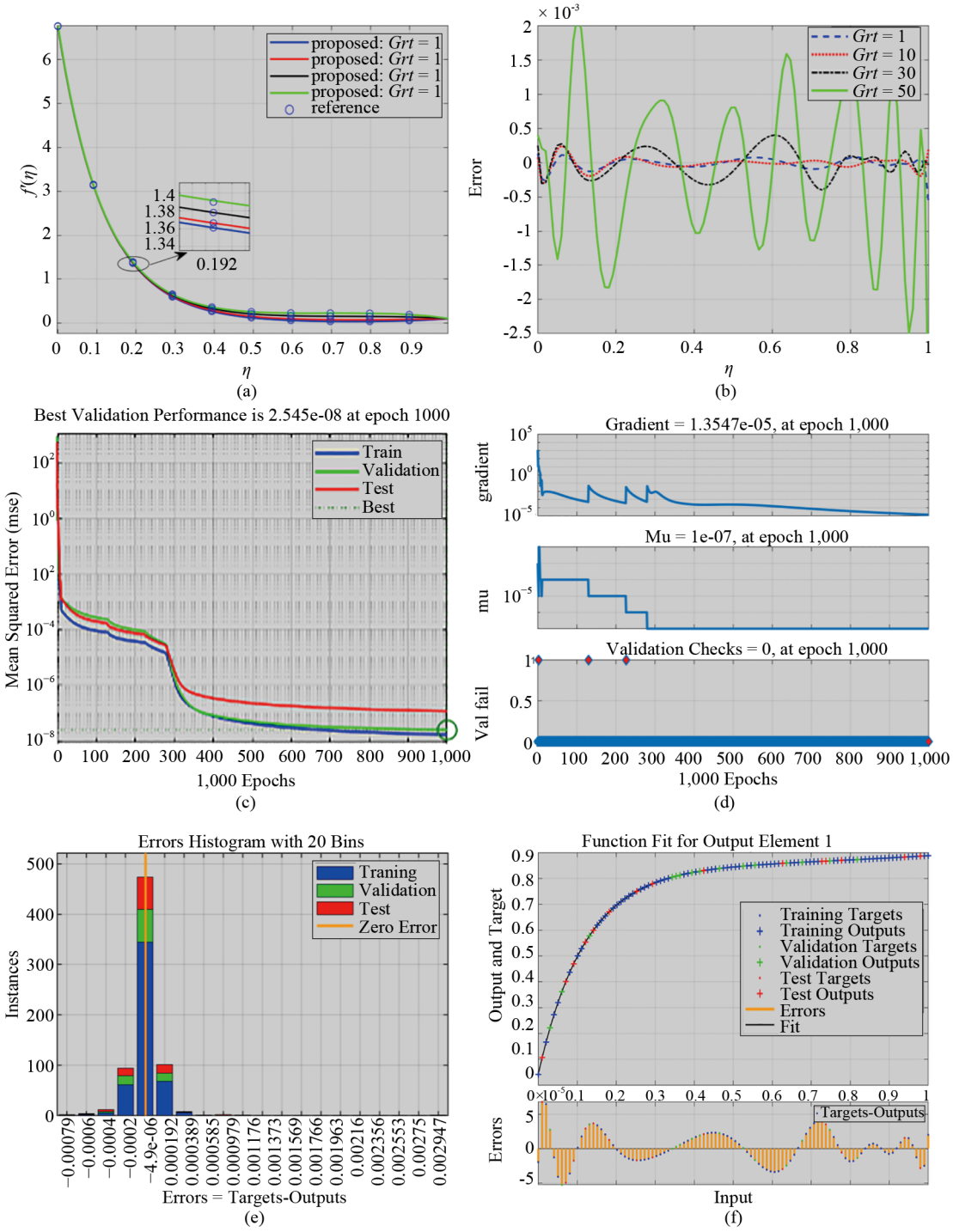

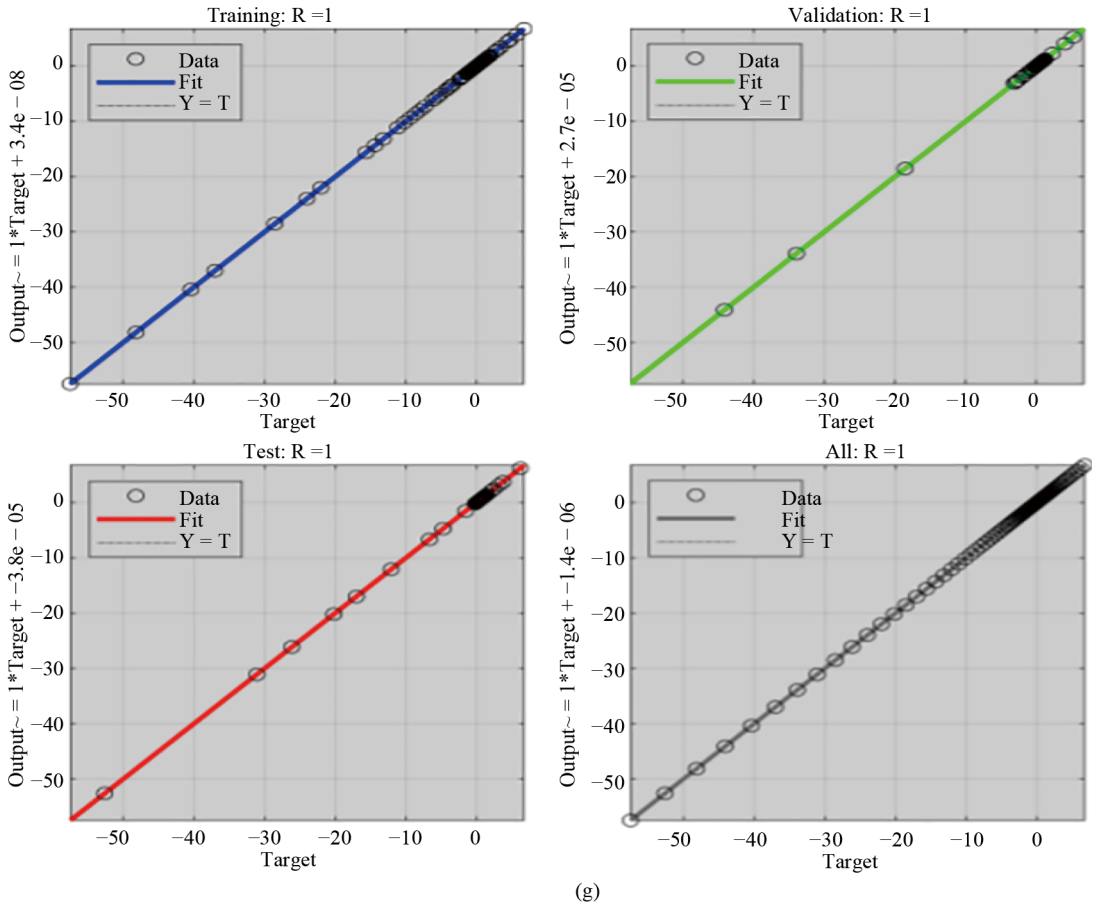

Figure 2. Comparison and error analysis of NN-BLMS with numerical results for G_{rt}: (a) impact on velocity (b) error analysis due to velocity (c) training result (d) comparison of training result (e) error histogram (f) curve fitting (g) regression

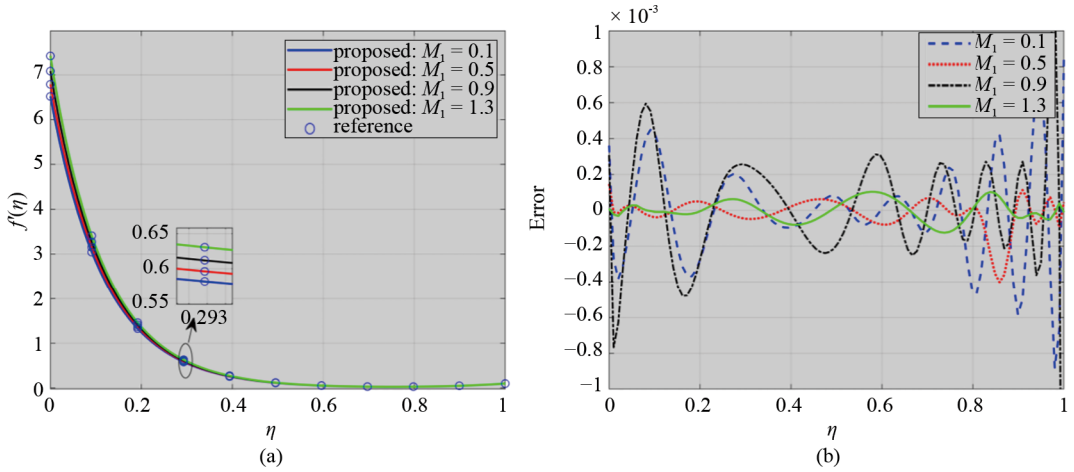

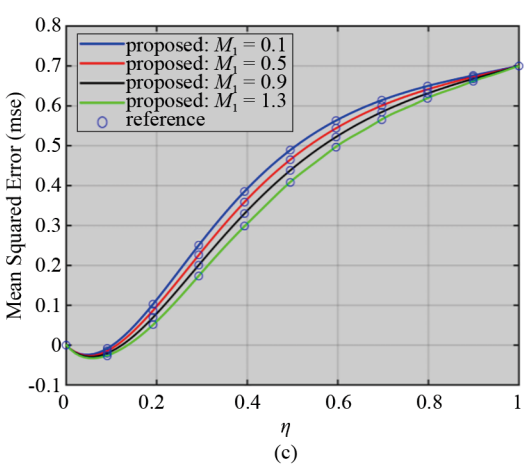
proposed: $M_1 = 0.1$
proposed: $M_1 = 0.5$
proposed: $M_1 = 0.9$
proposed: $M_1 = 1.3$
reference
Mean Squared Error (mse)
η

(c)

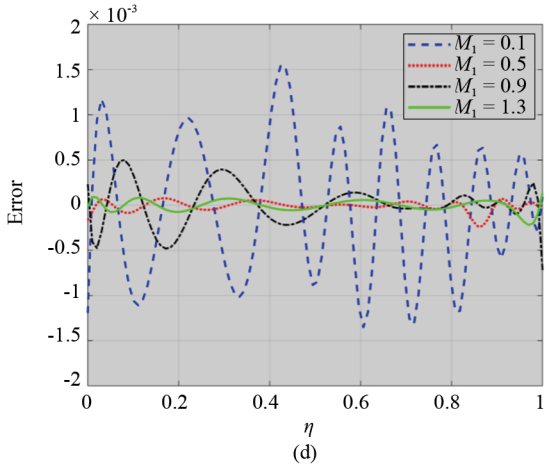
$\times 10^{-3}$
$M_1 = 0.1$
$M_1 = 0.5$
$M_1 = 0.9$
$M_1 = 1.3$
Error
η

(d)

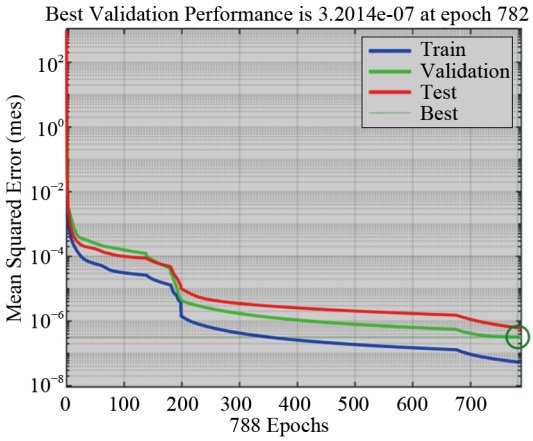
Best Validation Performance is 3.2014e-07 at epoch 782
Train
Validation
Test
Best
Mean Squared Error (mes)
788 Epochs

(e)

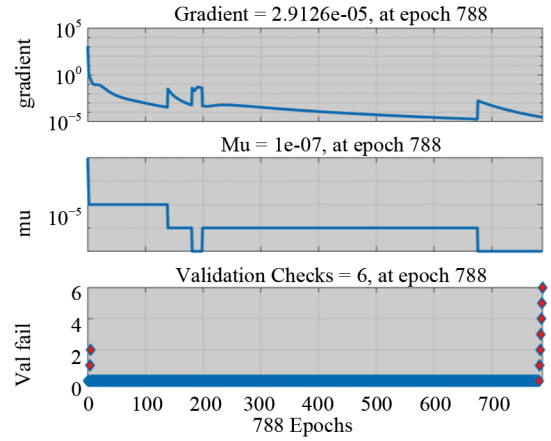
Gradient = 2.9126e-05, at epoch 788
gradient
Mu = 1e-07, at epoch 788
mu
Validation Checks = 6, at epoch 788
Val fail
788 Epochs

(f)

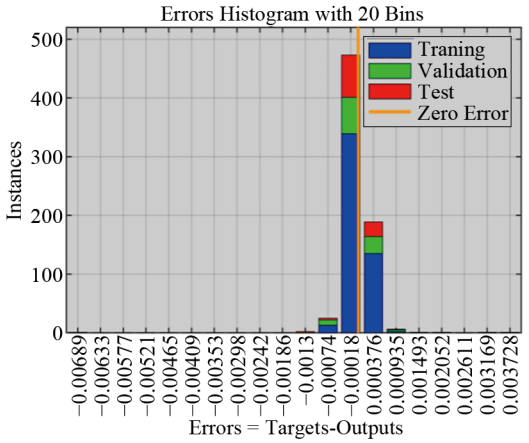
Errors Histogram with 20 Bins
Traning
Validation
Test
Zero Error
Instances
Errors = Targets-Outputs

(g)

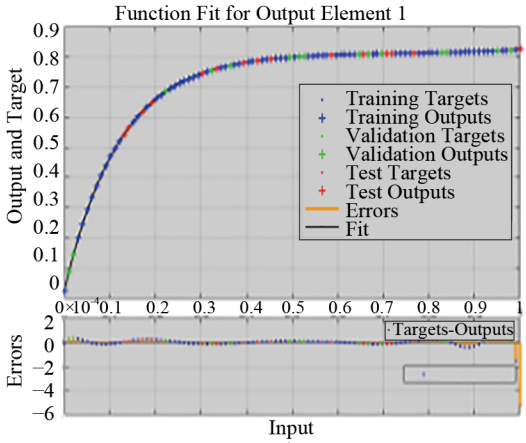
Function Fit for Output Element 1
Training Targets
Training Outputs
Validation Targets
Validation Outputs
Test Targets
Test Outputs
Errors
Fit
Output and Target
Targets-Outputs
Errors
Input

(h)

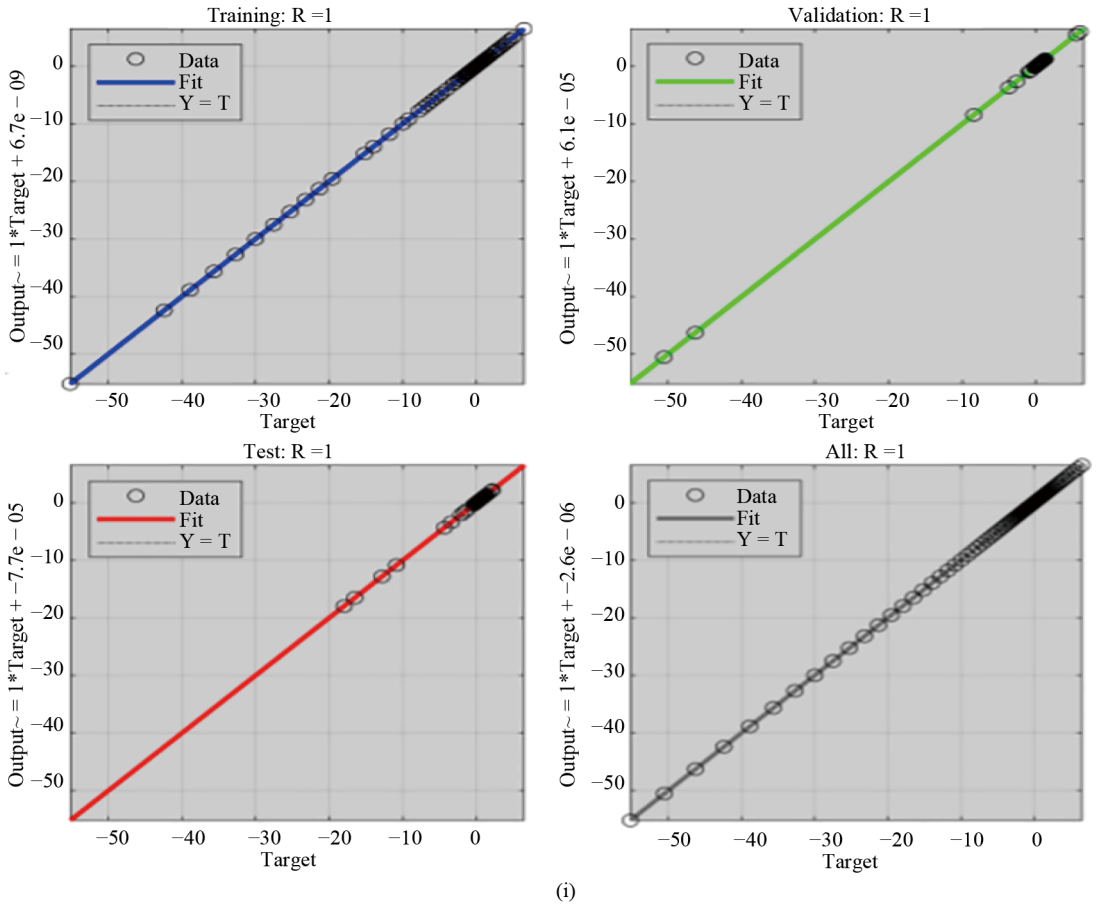

Figure 3. Comparison and error analysis of NN-BLMS with numerical results for M_1: (a) impact on velocity (b) error analysis due to velocity (c)impact on temperature (d) error analysis due to temperature (e) training result (f) comparison of training result (g) error histogram (h) curve fitting (i) regression

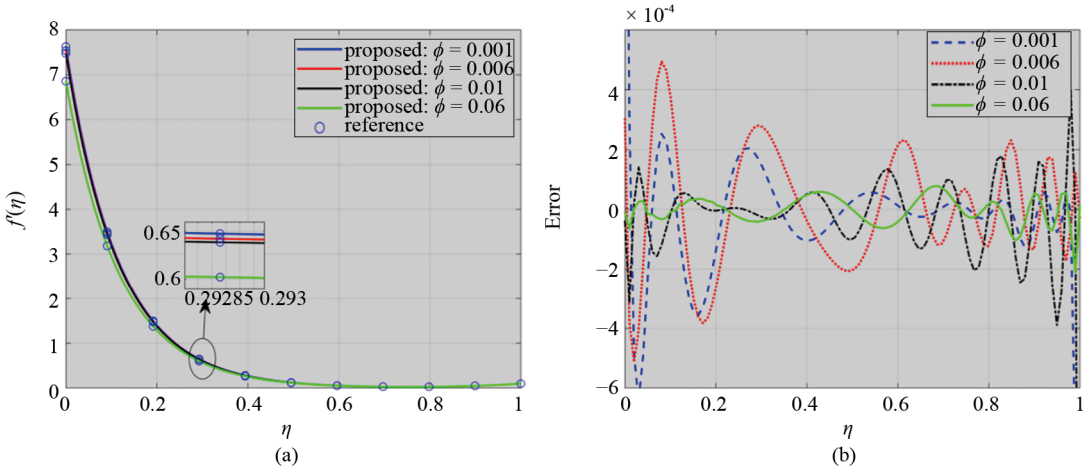

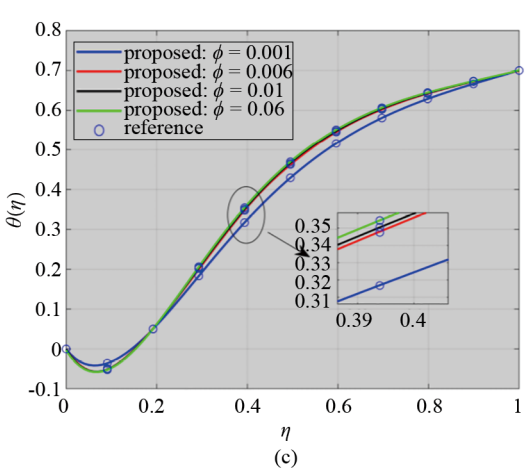
proposed: ϕ = 0.001
proposed: ϕ = 0.006
proposed: ϕ = 0.01
proposed: ϕ = 0.06
reference
$\theta(\eta)$
η

(c)

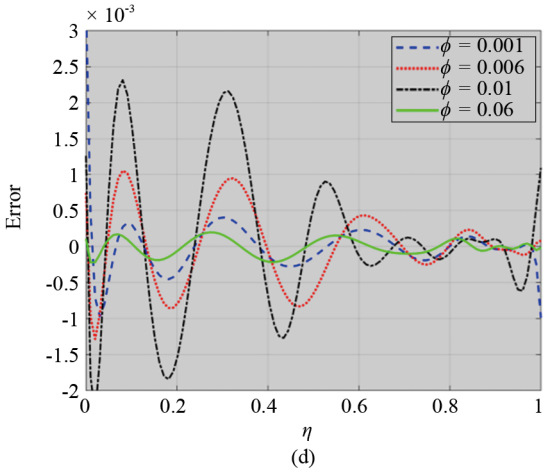
$\times 10^{-3}$
ϕ = 0.001
ϕ = 0.006
ϕ = 0.01
ϕ = 0.06
Error
η

(d)

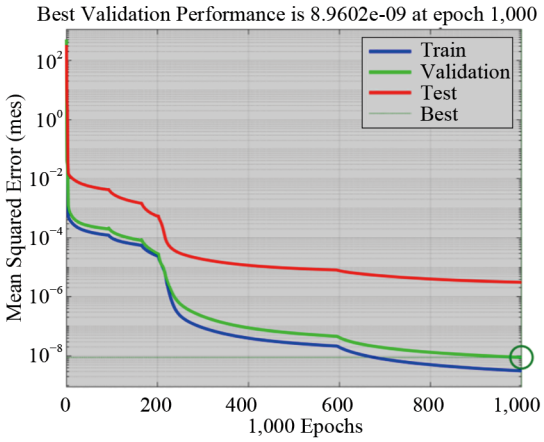
Best Validation Performance is 8.9602e-09 at epoch 1,000
Train
Validation
Test
Best
Mean Squared Error (mes)
1,000 Epochs

(e)

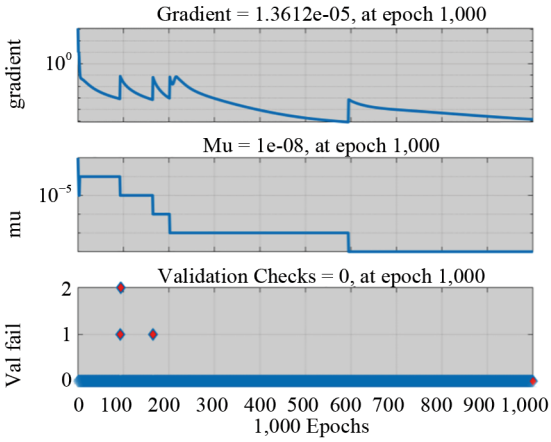
Gradient = 1.3612e-05, at epoch 1,000
gradient
Mu = 1e-08, at epoch 1,000
mu
Validation Checks = 0, at epoch 1,000
Val fail
1,000 Epochs

(f)

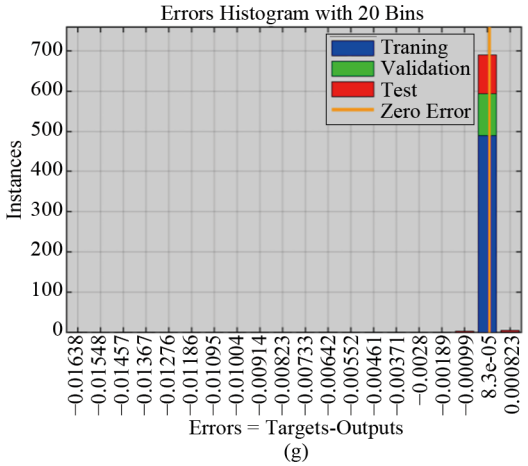
Errors Histogram with 20 Bins
Traning
Validation
Test
Zero Error
Instances
Errors = Targets-Outputs

(g)

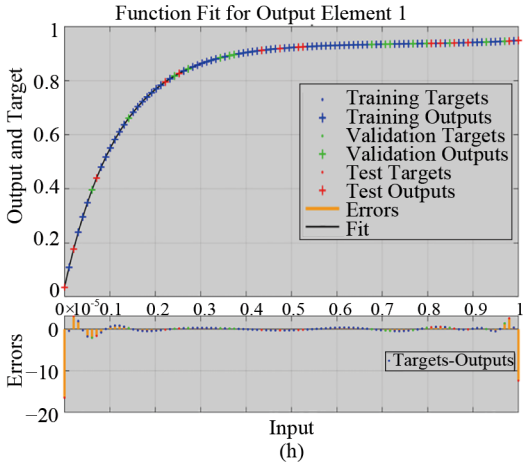
Function Fit for Output Element 1
Training Targets
Training Outputs
Validation Targets
Validation Outputs
Test Targets
Test Outputs
Errors
Fit
Output and Target
Targets-Outputs
Input

(h)

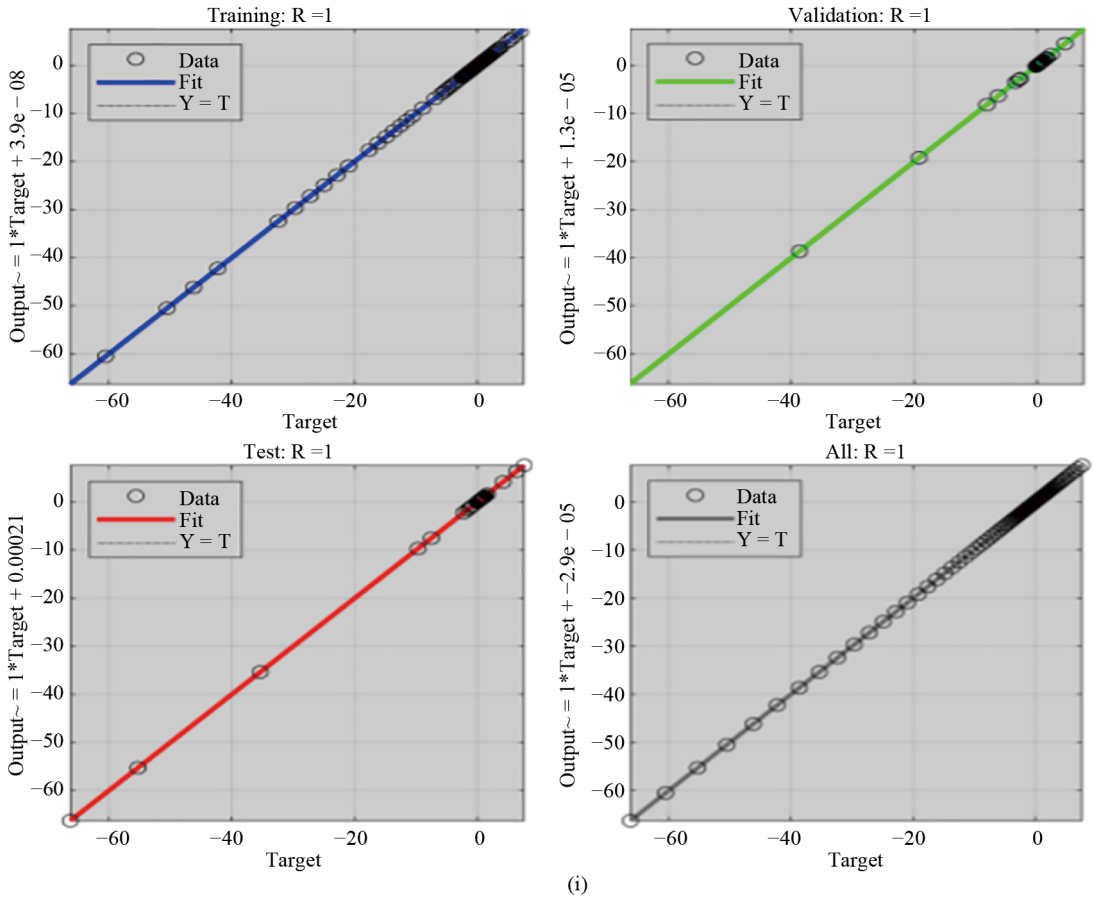

Figure 4. Comparison and error analysis of NN-BLMS with numerical results for ϕ: (a) impact on velocity (b) error analysis due to velocity (c)impact on temperature (d) error analysis due to temperature (e) training result (f) comparison of training result (g) error histogram (h) curve fitting (i) regression

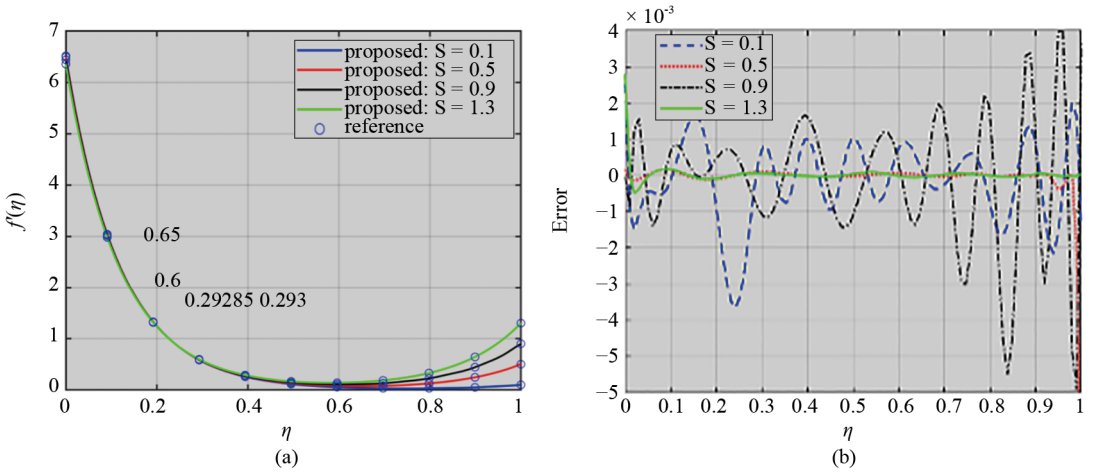

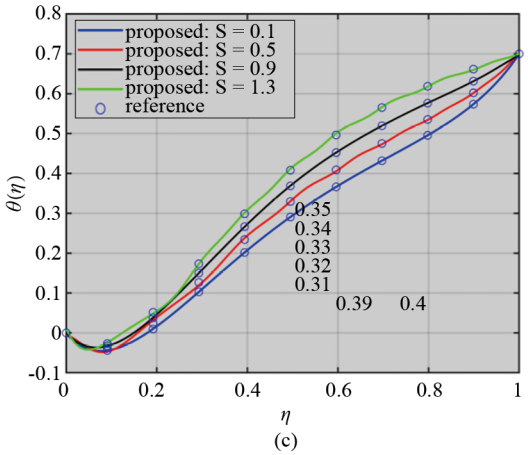
proposed: S = 0.1
proposed: S = 0.5
proposed: S = 0.9
proposed: S = 1.3
reference
θ(η)
η
0.35
0.34
0.33
0.32
0.31
0.39
0.4

(c)

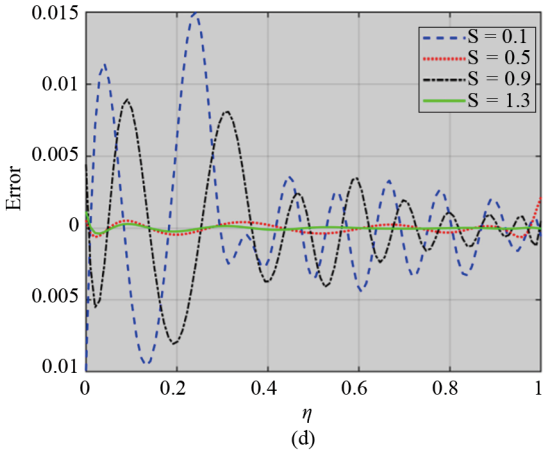
S = 0.1
S = 0.5
S = 0.9
S = 1.3
Error
η

(d)

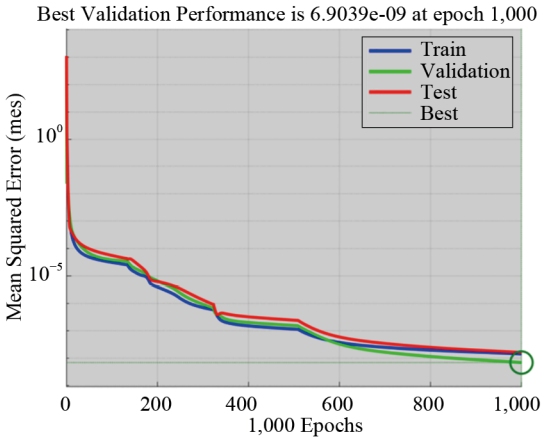
Best Validation Performance is 6.9039e-09 at epoch 1,000
Train
Validation
Test
Best
Mean Squared Error (mes)
1,000 Epochs

(e)

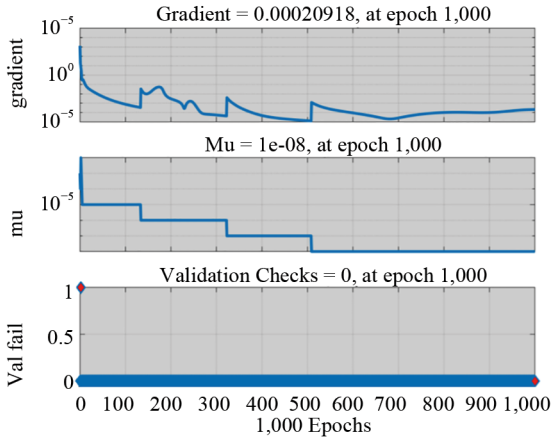
Gradient = 0.00020918, at epoch 1,000
gradient
Mu = 1e-08, at epoch 1,000
mu
Validation Checks = 0, at epoch 1,000
Val fail
1,000 Epochs

(f)

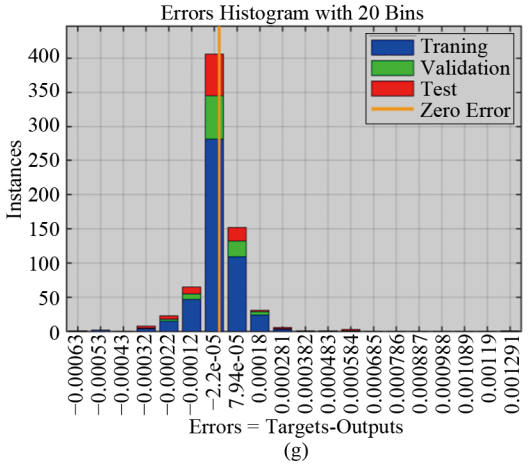
Errors Histogram with 20 Bins
Traning
Validation
Test
Zero Error
Instances
Errors = Targets-Outputs

(g)

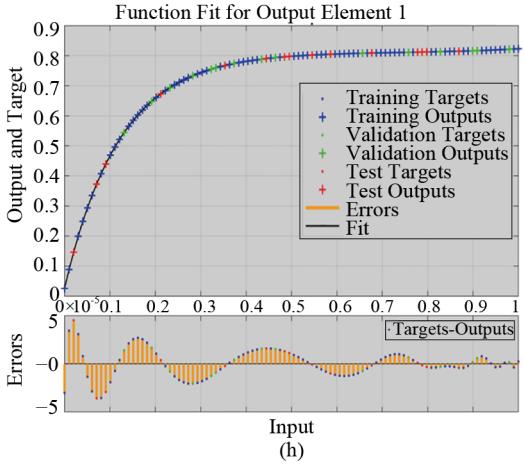
Function Fit for Output Element 1
Training Targets
Training Outputs
Validation Targets
Validation Outputs
Test Targets
Test Outputs
Errors
Fit
Output and Target
Targets-Outputs
Errors
Input

(h)

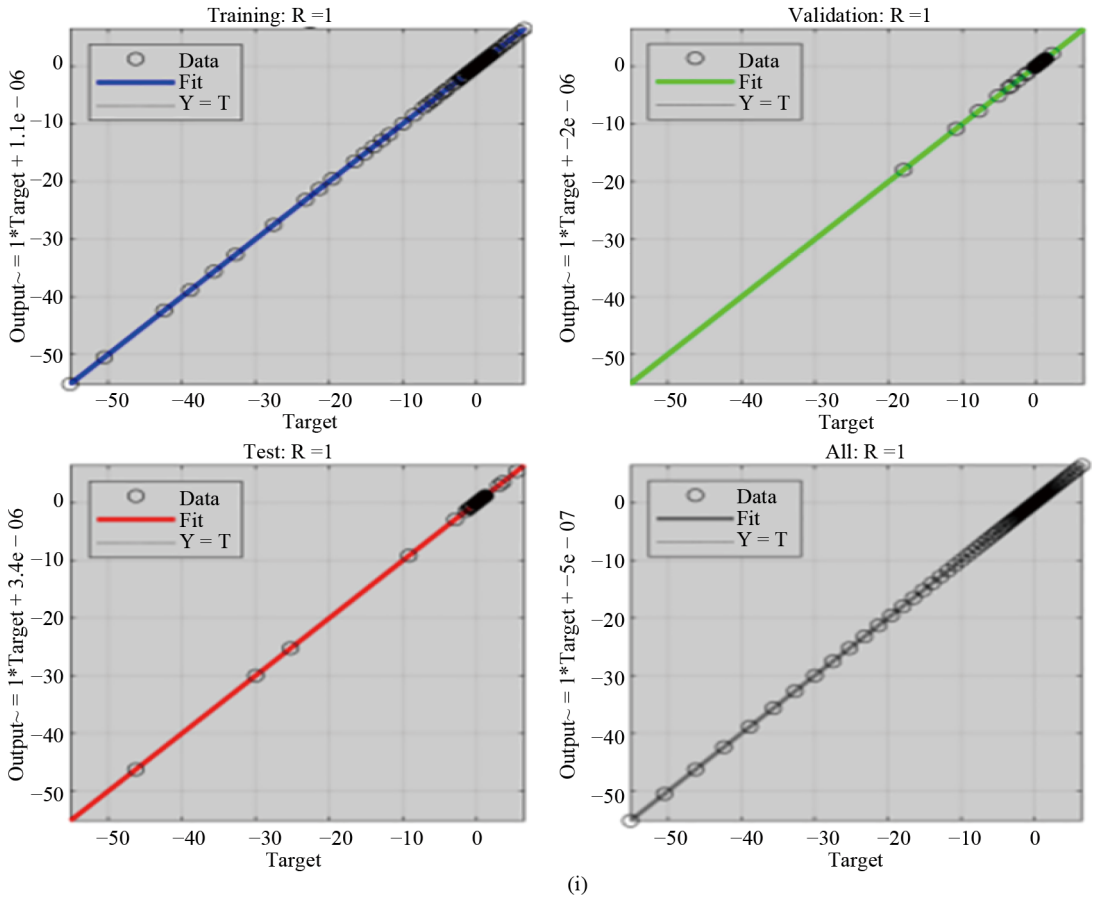

Figure 5. Comparison and error analysis of NN-BLMS with numerical results for *S*: (a) impact on velocity (b) error analysis due to velocity (c) impact on temperature (d) error analysis due to temperature (e) training result (f) comparison of training result (g) error histogram (h) curve fitting (i) regression

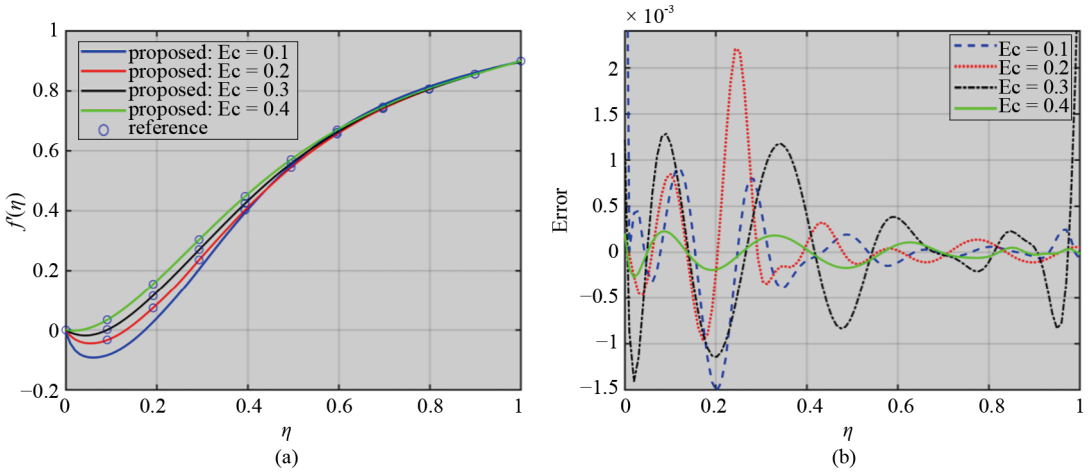

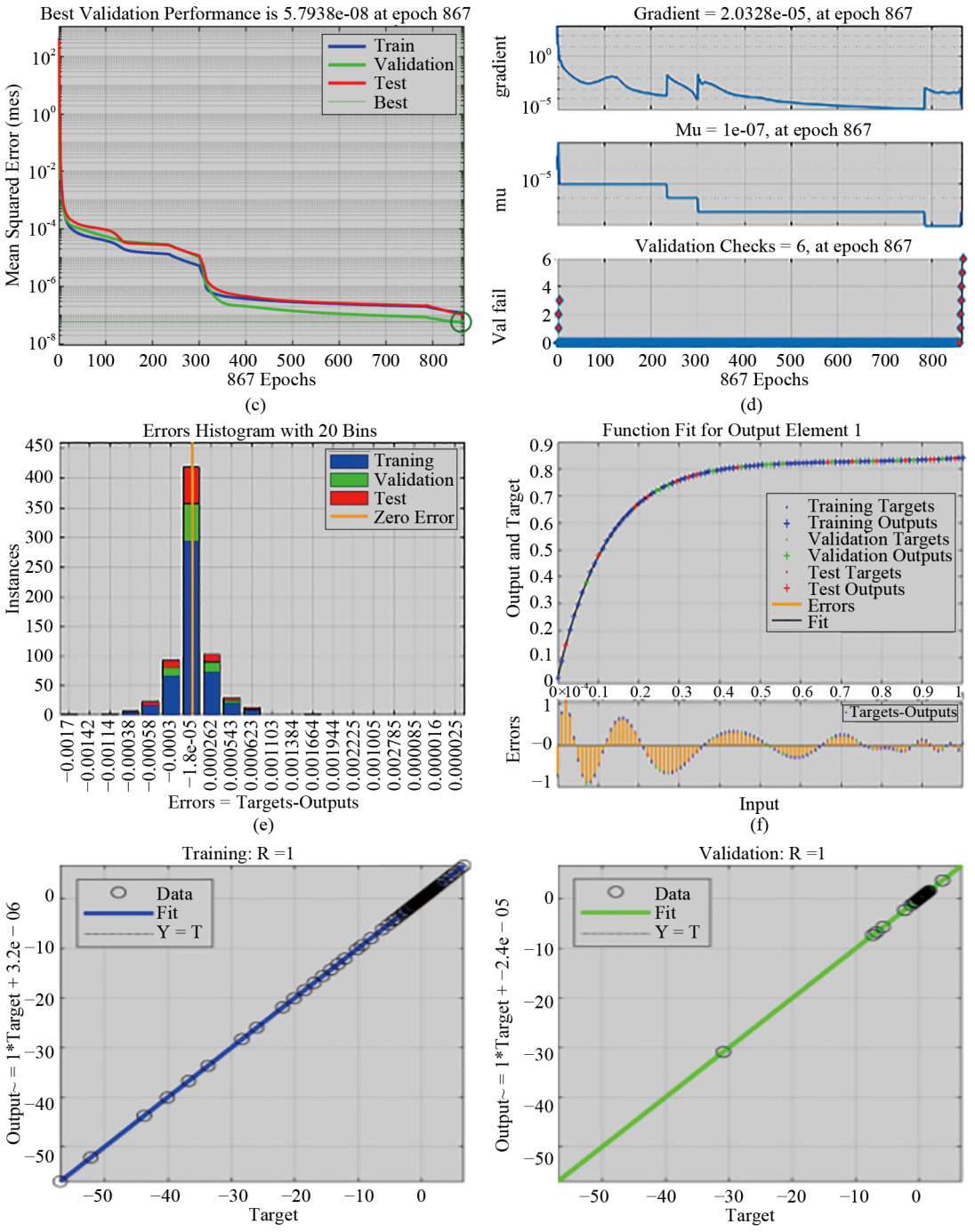
Best Validation Performance is 5.7938e-08 at epoch 867
Mean Squared Error (mes)
Train
Validation
Test
Best
867 Epochs
(c)
Gradient = 2.0328e-05, at epoch 867
gradient
Mu = 1e-07, at epoch 867
mu
Validation Checks = 6, at epoch 867
Val fail
867 Epochs
(d)
Errors Histogram with 20 Bins
Instances
Traning
Validation
Test
Zero Error
Errors = Targets-Outputs
(e)
Function Fit for Output Element 1
Output and Target
Training Targets
Training Outputs
Validation Targets
Validation Outputs
Test Targets
Test Outputs
Errors
Fit
Targets-Outputs
Input
(f)
Training: R =1
Output~ = 1*Target + 3.2e − 06
Data
Fit
Y = T
Target
Validation: R =1
Output~ = 1*Target + −2.4e − 05
Data
Fit
Y = T
Target

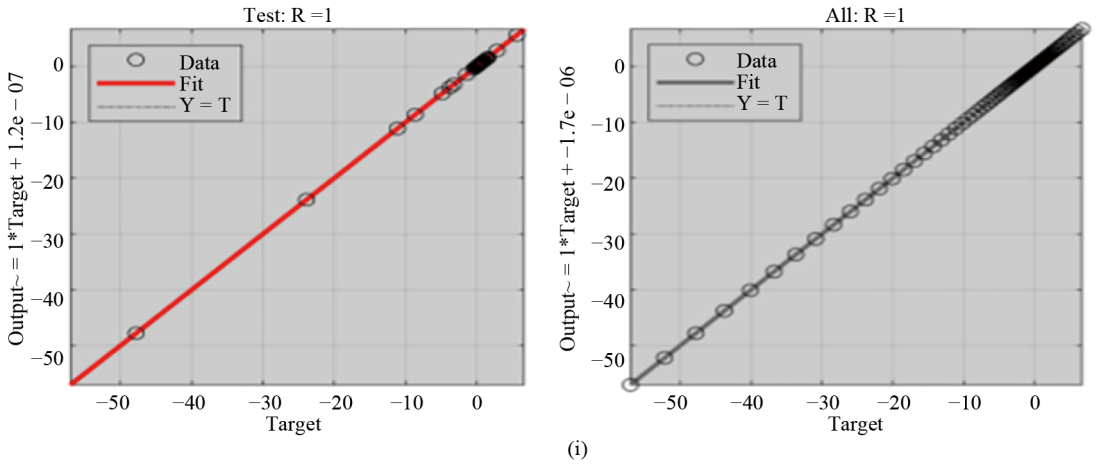

Figure 6. Comparison and error analysis of NN-BLMS with numerical results for *Ec*: (a) impact on velocity (b) error analysis due to velocity (c) training result (d) comparison of training result (e) error histogram (f) curve fitting (g) regression

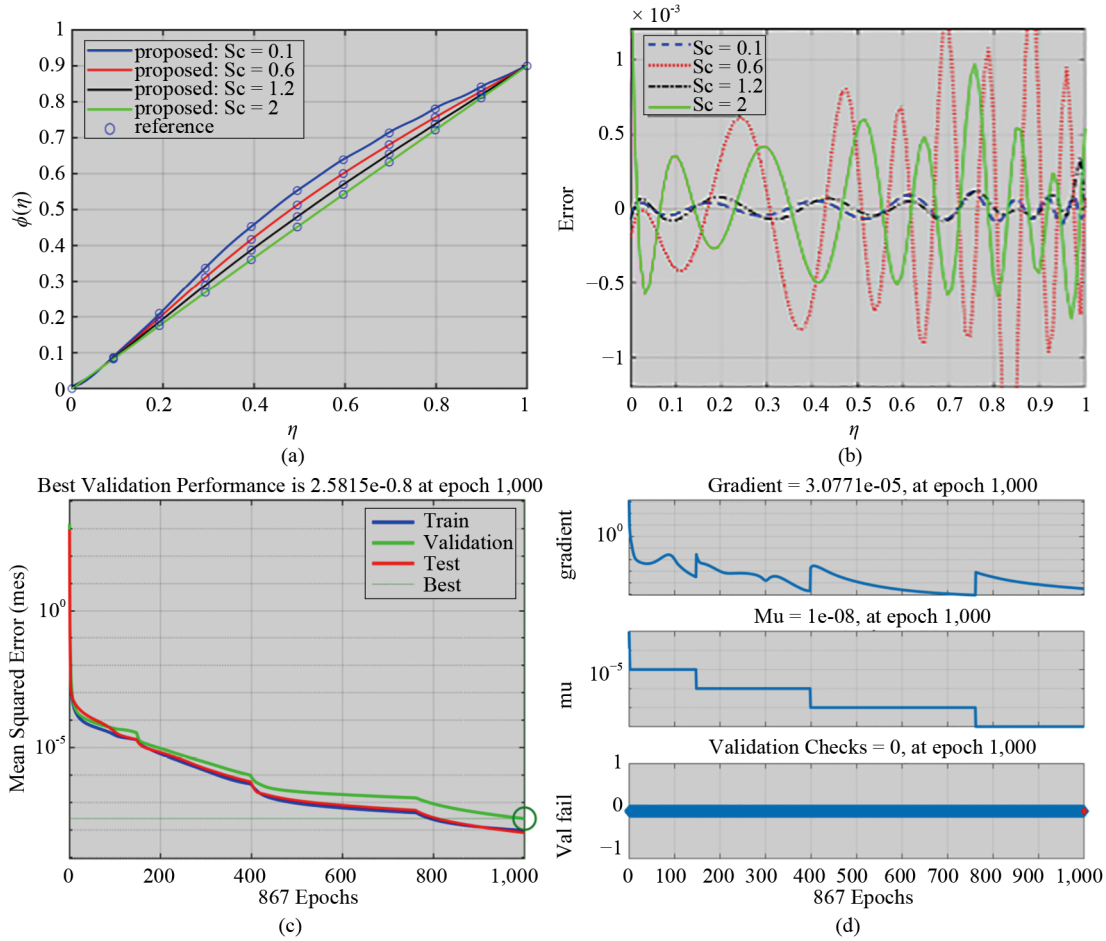

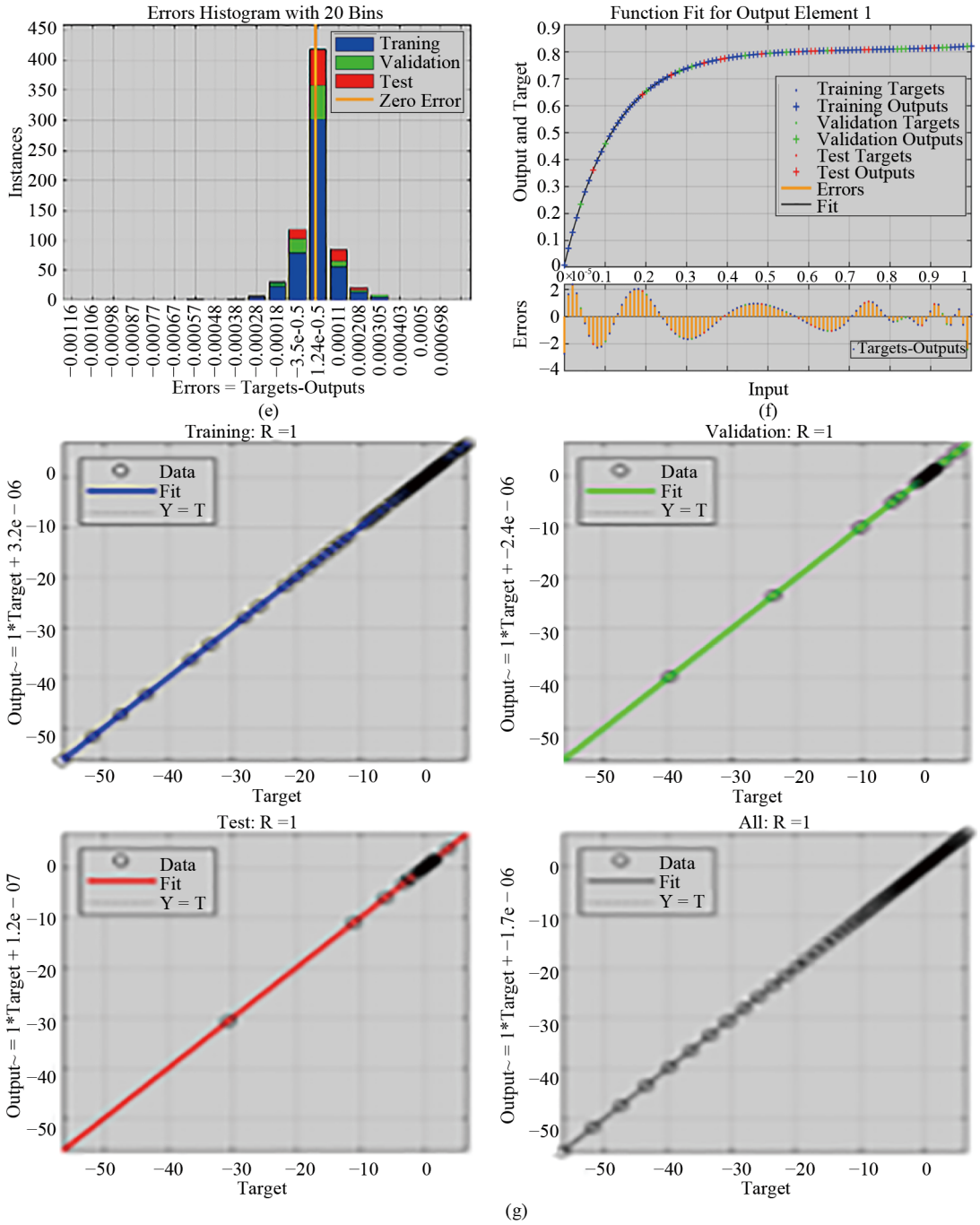

Figure 7. Comparison and error analysis of NN-BLMS with numerical results for *Sc*: (a) impact on velocity (b) error analysis due to velocity (c) training result (d) comparison of training result (e) error histogram (f) curve fitting (g) regression

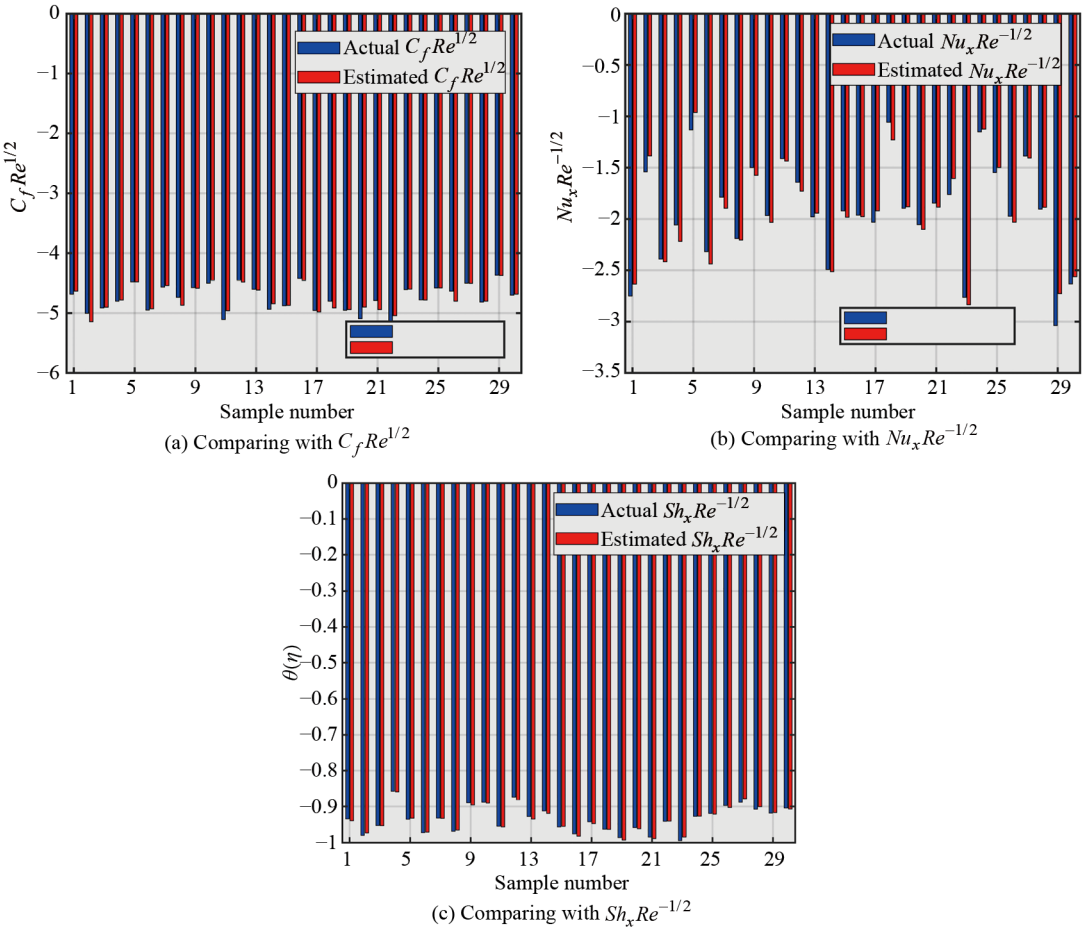

Figure 8. Comparison between actual and projected results

6. Conclusion

Finally, using a variable porosity and permeable media, we have examined the heat transfer of the ethyl acetate nanofluid flow with mixed convection phenomena and activation energy. We used the LMM-ABNNs technique with $4^{th}-$ order Runge Kutta numerical iteration to scrutinize heat and mass transportation. This article also explains the phenomena that come due to nanofluid with the latest ANN techniques and we hope our article is the best example to validate the performance, scrutinize the training and testing methods, and explore the validity of the approximate results. The final concluding remarks are given in the following order G_{rt}, M_1, ϕ, S, Ec, and Sc as follows:

- Velocity distribution profile increased as increasing of G_{rt}, M_1, S, Ec and decreased as increasing of ϕ and Sc.
- Error fluctuation are increased as increasing of G_{rt}, M_1, ϕ, S, Sc and decreased as increasing of Ec.
- Temperature distribution profile increased as increasing of ϕ, S and decreased as increasing of M_1. Similarly, for ϕ, S and M_1 error fluctuation are decreased.
- Best performance recorded at epochs $1,000$, 782, $1,000$, $1,000$, 861, $1,000$ with the MSE $e-08$, $e-06$, $e-08$, $e-08$, $e-08$, $e-07$, respectively.
- Gradient and Mu are $1.3547e-05$, $2.9125e-05$, $1.3612e-05$, $2.0918e-04$, $2.0328e-05$, $3.0771e-05$ and $1.0e-07$, $1.0e-07$, $1.0e-08$, $1.0e-08$, $1.0e-07$, $1.0e-08$ respectively in the given order.
- The height error for different data are $5e-05$, $5e-05$, $1.0e-05$, $5.0e-05$, $1.0e-04$ and $2.0e-05$ respectively.

Acknowledgement

The authors would like to acknowledge Deanship of Graduate Studies and Scientific Research, Taif University for funding this work.

Author contributions

Conceptualization, Aamir Farooq, Sadique Rehman, Mujahid Ullah, M.S. Abbas, K. El-Rashidy and Mohammad Kanan; Data curation, Mujahid Ullah; Formal analysis, Sadique Rehman and K. El-Rashidy; Investigation, Aamir Farooq, M.S. Abbas, K. El-Rashidy and M. Mamun Miah; Methodology, M.S. Abbas and M. Mamun Miah; Software, Aamir Farooq, M. Mamun Miah and Mohammad Kanan; Supervision, M. Mamun Miah and Mohammad Kanan; Validation, Sadique Rehman; Writing-original draft, Aamir Farooq, Sadique Rehman, Mujahid Ullah, M.S. Abbas and K. El-Rashidy; Writing-review and editing, M. Mamun Miah and Mohammad Kanan. All authors reviewed the manuscript.

Conflict of interest

The authors declare there is no conflict of interest at any point with reference to research findings.

References

[1] Drikakis D, Sofos F. Can artificial intelligence accelerate fluid mechanics research? *Fluids*. 2023; 8(7): 212.

[2] Kovani KG, Kontou MG, Asouti VG, Giannakoglou KC. DNN-driven gradient-based shape optimization in fluid mechanics. In: Lipu S, Williamson K, Lloyd A. (eds.) *International Conference on Engineering Applications of Neural Networks*. USA: Springer; 2023. p.379-390.

[3] Sharma P, Chung WT, Akoush B, Ihme M. A review of physics-informed machine learning in fluid mechanics. *Energies*. 2023; 16(5): 2343.

[4] Vinuesa R, Brunton SL, McKeon BJ. The transformative potential of machine learning for experiments in fluid mechanics. *Nature Reviews Physics*. 2023; 5(9): 536-545.

[5] Rehman S, Algarni S, Imtiaz M, Alqahtani T, ElSeabee FAA, Jamshed W, et al. Inclined magnetic force impact on cross nanoliquid flowing with widening shallow and heat generating by using artificial neural network (ANN). *Case Studies in Thermal Engineering*. 2023; 52(1): 103690.

[6] Ali I, Gul T, Khan A. Unsteady hydromagnetic flow over an inclined rotating disk through neural networking approach. *Mathematics*. 2023; 11(8): 1893.

[7] Prince HA, Ghosh A, Siam MMH, Mamun MAH. AI predicts MHD double-diffusive mixed convection and entropy generation in hybrid-nanofluids for different magnetic field inclination angles by ANN. *International Journal of Thermofluids*. 2023; 19: 100383. Available from: https://doi.org/10.1016/j.ijft.2023.100383.

[8] Reddy BAP, Jakeer S, Basha TH, Reddy RRS, Kumar M. Multi-layer artificial neural network modeling of entropy generation on MHD stagnation point flow of Cross-nanofluid. *Waves in Random and Complex Media*. 2022; 262: 1-28. Available from: https://doi.org/10.1080/17455030.2022.2067375.

[9] Muhammad S, Tabassum R, Khan MI, Raja MAZ, Khan NM. Neuro-computing-based Levenberg Marquardt algorithm for entropy optimized Darcy-Forchheimer nanofluid with variable viscosity. *Waves in Random and Complex Media*. 2022; 1-27. Available from: https://doi.org/10.1080/17455030.2022.2131013.

[10] Darvesh A, Altamirano GC. Inclined magnetic dipole and nanoscale energy exchange with infinite shear rate viscosity of 3D radiative cross nanofluid. *Heat Transfer*. 2022; 51(4): 3166-3186.

[11] Choi SUS. Nanofluids: From vision to reality through research. *Journal of Heat Transfer*. 2009; 131(3): 033106.

[12] Michaelides EE. Characteristics of nanofluids. In: *Nanofluidics: Thermodynamic and Transport Properties*. USA: Springer; 2014. p.47-90.

[13] Aamir F, Sadique R, Alharbi AN, Kamran M, Botmart T, Khan I. Closed-form solution of oscillating maxwell nano-fluid with heat and mass transfer. *Scientific Reports*. 2022; 12(1): 12205.

[14] Asghar A, Ying TY, Iqbal MJ, Ali L. Thermal characterization of hybrid nanofluid with impact of convective boundary layer flow and Joule heating law: Dual solutions case study. *Modern Physics Letters Bn*. 2023; 38(1): 19. Available from: https://doi.org/10.1016/j.amc.2014.03.072.

[15] Lin YJ, Rehman S, Akkurt N, Shedd T, Kamran M, Qureshi MI, et al. Free convective trickling over a porous medium of fractional nanofluid with MHD and heat source/sink. *Scientific Reports*. 2022; 12(1): 20778.

[16] Hussain SM, Imtiaz M, Bibi K, Rehman S, Jamshed W, Eid MR, et al. Error analysis of zirconium and zinc oxides/kerosene oil-based hybrid nanofluid flow between rotating disks: An innovative case study. *Case Studies in Thermal Engineering*. 2022; 51(8): 103549.

[17] Shah Z, Asghar A, Ying TY, Lund LA, Alshehri A, Vrinceanu N. Numerical investigation of sodium alginate-alumina/copper radiative hybrid nanofluid flow over a power law stretching/shrinking sheet with suction effect: A study of dual solutions. *Results in Engineering*. 2024; 21(5): 101881.

[18] Baloch LLA, Yashkun U, Shah NA. Multiple solutions of unsteady Darcy-Forchheimer porous medium flow of Cu-Al_2O_3/water based hybrid nanofluid with joule heating and viscous dissipation effect. *Journal of Thermal Analysis and Calorimetry*. 2024; 149(3): 2303-2315.

[19] Rasool G, Ahammad NA, Ali MR, Shah NA, Wang XH, Shafiq A, et al. Hydrothermal and mass aspects of MHD non-Darcian convective flows of radiating thixotropic nanofluids nearby a horizontal stretchable surface: Passive control strategy. *Case Studies in Thermal Engineering*. 2023; 42(749): 102654.

[20] Saleem S, Ahmad B, Naseem A, Riaz MB, Abbas T. Mono and hybrid nanofluid analysis over shrinking surface with thermal radiation: A numerical approach. *Case Studies in Thermal Engineering*. 2024; 54(2): 104023.

[21] Liaqat A, Retna A, Amir A, Priya T. Entropy generation on the dynamics of volume fraction of nano-particles and coriolis force impacts on mixed convective nanofluid flow with significant magnetic effect. *Numerical Heat Transfer, Part A: Applications*. 2024; 1-6. Available from: https://doi.org/10.1080/10407782.2024.2360652.

[22] Priya T, Hemant P, Sujesh A, Alphonsa M. Lie group analysis on EMHD Jeffrey nanofluid flow with exponential heat source: Heat transfer optimization using RSM. *Numerical Heat Transfer, Part B: Fundamentals*. 2024; 1-22. Available from: https://doi.org/10.1080/10407790.2024.2346932.

[23] Raza Q, Wang XD, Muhammed HAH, Ali B, Ali MR, Hendy AS. Numerically analyzed of ternary hybrid nanofluids flow of heat and mass transfer subject to various shapes and size factors in two-dimensional rotating porous channel. *Case Studies in Thermal Engineering*. 2023; 56(9): 104235.

[24] Raizah Z, Rehman S, Saeed A, Akbar M, Eldin SM, Galal AM. Melting rheology in thermally stratified graphene-mineral oil reservoir (third-grade nanofluid) with slip condition. *Nanotechnology Reviews*. 2023; 12(1): 20220511.

[25] Naqvi R, Manzoor U, Waqas H, Liu D, Naeem H, Eldin SM, et al. Numerical investigation of thermal radiation with entropy generation effects in hybrid nanofluid flow over a shrinking/stretching sheet. *Journal of Thermal Analysis and Calorimetry*. 2024; 13(1): 20230171.

[26] Lone SA, Raizah Z, Shah MH, Rehman S, Saeed A, Eldin SM. Thermal and solutal slips impact on 3D-biconvection flow of linearly stratified Casson nanofluid (magnesium-blood) passed over a bi-stretching surface in a rotating frame. *Results in Physics*. 2023; 55: 107139. Available from: https://doi.org/10.1016/j.rinp.2023.107139.

[27] Algehyne E, Haq I, Rehman S, Raizah Z, Saeed A, Galal AM. Computational assessment of thermally stratified magnetohydrodynamics maxwell nanofluid with joule heating and melting heat transfer. *Results in Physics*. 2023; 50(2): 5897-5916.

[28] Ganie A, Albaidani M, Farooq S, Rehman S, Farooq A, Z DF, et al. Analysis of thermally stratified micropolar carreau-yasuda hybrid nanofluid flow with cattaneo-christov heat and mass flux. *Journal of Thermal Analysis and Calorimetry*. 2023; 148(13): 106542.

[29] Zafar SS, Zaib A, Ali F, Alduais FS, Bossly AA, Saeed A. Second law analysis on Ree-Eyring nanoliquid and Darcy Forchheimer flow through a significant stratification in the gyrotactic microorganism. *International Journal of Numerical Methods for Heat & Fluid Flow*. 2024; 34(2): 494-519.

[30] Leng YC, Li SG, Algarni S, Jamshed W, Alqahtani T, Ibrahim RW, et al. Computational study of magnetized and dual stratified effects on Non-Darcy Casson nanofluid flow: An activation energy analysis. *Case Studies in Thermal Engineering*. 2024; 53(1): 103804.

[31] Debnath P, Pradhan M. Numerical simulation on heat transfer enhancement and design optimization of modified SCTHX using Taguchi method. *AIP Conference Proceedings*. 2023; 2943(1): 020021. Available from: https://doi.org/10.1063/5.0183130.

[32] Das D, Shaw S, Kairi RR. Irreversibility estimation in triply stratified bio-marangoni convection in powell-eyring nanofluid under the influence of external flow. *Physica Scripta*. 2024; 99(5): 055253.

[33] Saif RS, Muhammad T, Sadia H. Significance of inclined magnetic field in darcy-forchheimer flow with variable porosity and thermal conductivity. *Physica Scripta*. 2020; 551: 124067. Available from: https://doi.org/10.1016/j.physa.2019.124067.

[34] Farooq M, Anjum A, Anwer A, Malik MY. Convective transportation in thermally stratified tween-20-water/ethyl acetate fluid reservoirs constraint to riga surface. *International Communications in Heat and Mass Transfer*. 2022; 138: 106271. Available from: https://doi.org/10.1016/j.icheatmasstransfer.2022.106271.

[35] Prakash D, Muthtamilselvan M, Doh DH. Unsteady MHDnon-darcian flow over avertical stretching plate embedded in a porous medium with non-uniform heat generation. *Applied Mathematics and Computation*. 2014; 236: 480-492. Available from: https://doi.org/10.1016/j.amc.2014.03.072.

[36] Cleve M. MATLAB-mathWorks. 2024. Available from: https://ww2.mathworks.cn/en/products/matlab.html.